

# Node-based uniform strain virtual elements for compressible and nearly incompressible plane elasticity

A. Ortiz-Bernardin<sup>a,\*</sup>, R. Silva-Valenzuela<sup>a</sup>, S. Salinas-Fernández<sup>b</sup>, N. Hitschfeld-Kahler<sup>b</sup>, S. Luza<sup>a</sup>, B. Rebolledo<sup>a</sup>

<sup>a</sup>*Computational and Applied Mechanics Laboratory, Department of Mechanical Engineering, Universidad de Chile, Av. Beauchef 851, Santiago 8370456, Chile.*

<sup>b</sup>*Department of Computer Science, Universidad de Chile, Av. Beauchef 851, Santiago 8370456, Chile.*

---

## Abstract

We propose a combined nodal integration and virtual element method for compressible and nearly incompressible plane elasticity, wherein the strain is averaged at the nodes from the strain of surrounding virtual elements. For the strain averaging procedure, a nodal averaging operator is constructed using a generalization to virtual elements of the node-based uniform strain approach for finite elements. We refer to these new elements as node-based uniform strain virtual elements (NVEM). No additional degrees of freedom are introduced in this approach, thus resulting in a displacement-based formulation. A salient feature of the NVEM is that the stresses and strains become nodal variables just like displacements, which can be exploited in nonlinear simulations. Through several benchmark problems in plane elasticity, we demonstrate that the NVEM is accurate and optimally convergent, and devoid of volumetric locking in the nearly incompressible limit.

*Keywords:* Virtual element method, Nodal integration, Strain averaging, Uniform strain, Linear elasticity, Volumetric locking

---

## 1. Introduction

We propose a combined nodal integration and virtual element method (VEM) for compressible and nearly incompressible plane elasticity, wherein the strain is averaged at the nodes from the

---

\*Corresponding author. Tel: +56 2 2978 4664, Fax: +56 2 2689 6057,  
*Email address:* aortizb@uchile.cl (A. Ortiz-Bernardin)

strain of surrounding virtual elements. The proposed method differs from existing virtual element methods for compressible and nearly incompressible elasticity in the following aspects:

- In the proposed approach, the volumetric locking is alleviated by the strain averaging at the nodes and the stabilization matrix chosen. No additional degrees of freedom are introduced in this approach, thus resulting in a displacement-based formulation. In the existing VEM approaches, the volumetric locking is alleviated by the B-bar formulation [1, 2], mixed formulation [3], enhanced strain formulation [4], hybrid formulation [5], nonconforming formulations [6–8], or addition of degrees of freedom related to the normal components of the displacement field on the element’s edges to satisfy the inf-sup condition [9].
- The strains and stresses in the proposed approach are projected to the nodes, thus becoming nodal quantities just like displacements, whereas in the existing approaches these are projected inside the elements, thus becoming element quantities.

Nodal integration can be traced back to the work of Beissel and Belytschko [10] for meshfree Galerkin methods, where nodal integration emerged as an alternative to Gauss integration to accelerate the numerical integration of the weak form integrals. The main difference between these two types of numerical integration is that in nodal integration the weak form integrals are sampled at the nodes, whereas in Gauss integration the integrals are numerically integrated in the interior of the elements using cubature. Thus, in nodal integration, the state and history-dependent variables in the weak form integrals naturally become nodal quantities, whereas in Gauss integration these variables become element quantities. The obvious advantages of nodal integration over Gauss integration can be summarized as follows. There are much less nodes than Gauss points in the mesh, which results in huge computational savings when nodal integration is employed. In nonlinear computations with nodally integrated weak form integrals, the state and history-dependent variables are tracked only at the nodes. This feature can be exploited to avoid mesh remapping of these variables in Lagrangian large deformation simulations with remeshing (see, for instance, [11]), which is not possible when Gauss integration is used.

After the work of Beissel and Belytschko [10] nodal integration attracted great interest from the meshfree community (e.g., see Refs. [12–22]) due to the improved robustness of this type of

integration over cell-based Gauss integration. Even though nodal integration greatly improves the computational cost of meshfree Galerkin simulations, still there exists the computational burden of meshfree basis functions (e. g., moving least-squares [23, 24], reproducing kernel [25] and maximum-entropy [26–28] approximants), which includes the solution of an optimization problem and a neighbor search at every integration node. Besides, meshfree basis functions generally do not vanish on the boundary, which requires additional procedures to impose Dirichlet boundary conditions. Regarding finite elements, there are various nodal integration approaches that use some form of pressure or strain averaging at the nodes; for instance, the average nodal pressure tetrahedral element [29], node-based uniform strain triangular and tetrahedral elements [30], the averaged nodal deformation gradient linear tetrahedral element [31], and the family of nodally integrated continuum elements (NICE) and its derivative approaches [32–35, 35–38]. Recently, the node-based uniform strain approach [30] was adopted in the nodal particle finite element method (NPFEM) [39, 40].

Nodal integration is prone to instabilities, and thus it requires stabilization. Stabilization is also an important aspect within the theoretical framework of the VEM <sup>1</sup>, and thus this represents the main connection between nodal integration and the virtual element method. A summary of the stability issue in nodal integration is provided in Ref. [11], where also a gradient-based stabilization is proposed for small and Lagrangian large deformation simulations.

The VEM allows direct imposition of Dirichlet boundary conditions and its computational cost is comparable to that of the finite element method [43]. In addition, it is equipped with a stabilization procedure like in nodal integration. Regarding its sensitivity to mesh distortions, several authors have reported very robust solutions under mesh distortions [1, 44–48] and highly nonconvex elements [2, 49–51]. Therefore, it is our opinion that the VEM will play a key role in the development of robust nodal integration techniques, especially in extreme large deformations.

In this exploratory paper, a combined nodal integration and virtual element method is proposed using ideas taken from the node-based uniform strain approach of Dohrmann et al. [30] for finite elements, wherein the strain is averaged at the nodes from the strain of surrounding elements. We

---

<sup>1</sup>Although stabilization-free virtual elements were recently proposed [41, 42].

refer to these new elements as node-based uniform strain virtual elements (NVEM). The focus in this paper is on plane elasticity, whose governing equations are provided in Section 2. Section 3 summarizes the theoretical framework of the VEM for plane elasticity. Node-based uniform strain virtual elements are developed in Section 4. Stabilizations for the NVEM are discussed in Section 5. In Section 6, the numerical behavior of the NVEM is examined through several benchmark problems in compressible and nearly incompressible elasticity. Some concluding remarks along with ongoing and future research directions are discussed in Section 7. To ease the reading of the equations, a list of main symbols used throughout the paper is provided in Appendix A.

## 2. Governing equations

Consider an elastic body that occupies the open domain  $\Omega \subset \mathbb{R}^2$  and is bounded by the one-dimensional surface  $\Gamma$  whose unit outward normal is  $\mathbf{n}_\Gamma$ . The boundary is assumed to admit decompositions  $\Gamma = \Gamma_D \cup \Gamma_N$  and  $\emptyset = \Gamma_D \cap \Gamma_N$ , where  $\Gamma_D$  is the Dirichlet boundary and  $\Gamma_N$  is the Neumann boundary. The closure of the domain is  $\overline{\Omega} = \Omega \cup \Gamma$ . Let  $\mathbf{u}(\mathbf{x}) : \overline{\Omega} \rightarrow \mathbb{R}^2$  be the displacement field at a point of the elastic body with position vector  $\mathbf{x}$  when the body is subjected to external tractions  $\mathbf{t}_N(\mathbf{x}) : \Gamma_N \rightarrow \mathbb{R}^2$  and body forces  $\mathbf{b}(\mathbf{x}) : \Omega \rightarrow \mathbb{R}^2$ . The imposed Dirichlet (essential) boundary conditions are  $\mathbf{u}_D(\mathbf{x}) : \Gamma_D \rightarrow \mathbb{R}^2$ . The boundary-value problem for linear elastostatics reads: find  $\mathbf{u}(\mathbf{x}) : \overline{\Omega} \rightarrow \mathbb{R}^2$  such that

$$\nabla \cdot \boldsymbol{\sigma} + \mathbf{b} = 0 \quad \text{in } \Omega, \quad (1a)$$

$$\mathbf{u} = \mathbf{u}_D \quad \text{on } \Gamma_D, \quad (1b)$$

$$\boldsymbol{\sigma} \cdot \mathbf{n}_\Gamma = \mathbf{t}_N \quad \text{on } \Gamma_N, \quad (1c)$$

where  $\boldsymbol{\sigma}$  is the Cauchy stress tensor.

The Galerkin weak formulation of the above problem is: find  $\mathbf{u}(\mathbf{x}) \in \mathcal{V}$  such that

$$\begin{aligned} a(\mathbf{u}, \mathbf{v}) &= \ell(\mathbf{v}) \quad \forall \mathbf{v}(\mathbf{x}) \in \mathcal{W}, \\ a(\mathbf{u}, \mathbf{v}) &= \int_{\Omega} \boldsymbol{\sigma}(\mathbf{u}) : \boldsymbol{\varepsilon}(\mathbf{v}) \, d\mathbf{x}, \quad \ell(\mathbf{v}) = \int_{\Omega} \mathbf{b} \cdot \mathbf{v} \, d\mathbf{x} + \int_{\Gamma_N} \mathbf{t}_N \cdot \mathbf{v} \, ds, \end{aligned} \quad (2)$$

where  $\mathcal{V}$  denotes the space of admissible displacements and  $\mathcal{W}$  the space of its variations, and  $\boldsymbol{\varepsilon}$  is the small strain tensor that is given by

$$\boldsymbol{\varepsilon}(\mathbf{u}) = \frac{1}{2}(\mathbf{u} \otimes \boldsymbol{\nabla} + \boldsymbol{\nabla} \otimes \mathbf{u}). \quad (3)$$

### 3. Virtual element method for plane elasticity

The virtual element method (VEM) [52] is a generalization of the finite element method (FEM) that can deal with very general meshes formed by elements with arbitrary number of edges (convex or non-convex polygons); the mesh can even include elements with coplanar edges and collapsing nodes, and non-matching elements. In the VEM, the displacement field is decomposed into a polynomial part and other terms by using a projection operator. Altogether, this procedure results in no explicit computation of basis functions (basis functions are *virtual*) and an algebraic construction of the element stiffness matrix. The decomposition of the displacement field leads to the following decomposition of the virtual element stiffness matrix:

$$\mathbf{K}_E = \mathbf{K}_E^c + \mathbf{K}_E^s, \quad (4)$$

where  $\mathbf{K}_E^c$  is the consistency part of the element stiffness matrix, which provides consistency to the method (i.e., ensures patch test satisfaction), and  $\mathbf{K}_E^s$  is the stability part of the element stiffness matrix, which provides stability.

A brief summary of the VEM for plane elasticity is given next. All the derivations are presented at the element level. Concerning the element, the following notation is used: the element is denoted by  $E$  and its boundary by  $\partial E$ . The area of the element is denoted by  $|E|$ . The number of edges/nodes of an element are denoted by  $N_E^V$ . The unit outward normal to the element boundary in the Cartesian coordinate system is denoted by  $\mathbf{n} = [n_1 \quad n_2]^T$ . Fig. 1 depicts an element with five edges ( $N_E^V = 5$ ), where the edge  $e_a$  of length  $|e_a|$  and the edge  $e_{a-1}$  of length  $|e_{a-1}|$  are the element edges incident to node  $a$ , and  $\mathbf{n}_a$  and  $\mathbf{n}_{a-1}$  are the unit outward normals to these edges, respectively.

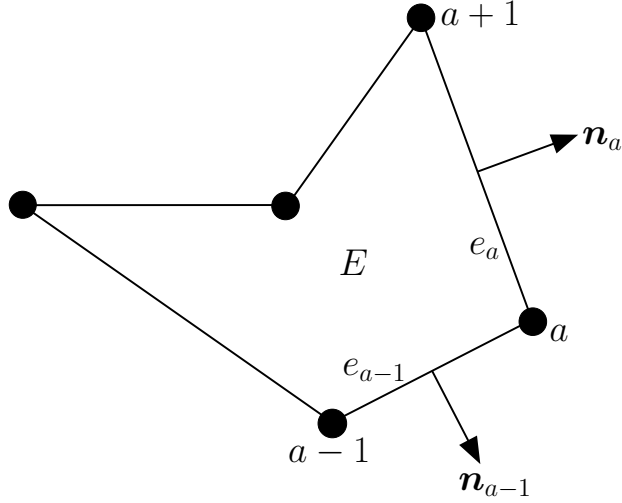


Fig. 1: Schematic representation of a polygonal element of  $N_E^V = 5$  edges.

### 3.1. Projection operator

The fundamental procedure in the VEM is the decomposition of the displacement field into its polynomial part and some additional terms that are generally nonpolynomials. To this end, a projection operator  $\Pi$  is defined such that

$$\mathbf{u}_h = \Pi \mathbf{u}_h + (\mathbf{u}_h - \Pi \mathbf{u}_h), \quad (5)$$

where  $\mathbf{u}_h$  is displacement approximation on the element (trial function),  $\Pi \mathbf{u}_h$  is the polynomial part of  $\mathbf{u}_h$  and  $\mathbf{u}_h - \Pi \mathbf{u}_h$  contains the nonpolynomial terms of  $\mathbf{u}_h$ .

In this paper, we restrict ourselves to low-order approximations; that is,  $\Pi$  is meant to project onto the space of linear polynomials. Let  $\mathbf{x}_a = [x_{1a} \ x_{2a}]^\top$  and  $\mathbf{u}_a = [u_{1a} \ u_{2a}]^\top$  be the coordinates and displacements of node  $a$ , respectively. At the element level, the projection operator onto the

linear displacements can be defined as [21, 43, 53, 54]

$$H\mathbf{u}_h = \begin{bmatrix} (x_1 - \bar{x}_1) & 0 & \frac{1}{2}(x_2 - \bar{x}_2) & 1 & 0 & \frac{1}{2}(x_2 - \bar{x}_2) \\ 0 & (x_2 - \bar{x}_2) & \frac{1}{2}(x_1 - \bar{x}_1) & 0 & 1 & -\frac{1}{2}(x_1 - \bar{x}_1) \end{bmatrix} \begin{bmatrix} \hat{\varepsilon}_{11} \\ \hat{\varepsilon}_{22} \\ 2\hat{\varepsilon}_{12} \\ \bar{u}_1 \\ \bar{u}_2 \\ 2\hat{\omega}_{12} \end{bmatrix}, \quad (6)$$

where  $\bar{x}_1$  and  $\bar{x}_2$  are the components of the mean of the values that the position vector  $\mathbf{x}$  takes over the vertices of the element; i.e.,

$$\bar{\mathbf{x}} = \begin{bmatrix} \bar{x}_1 \\ \bar{x}_2 \end{bmatrix} = \frac{1}{N_E^V} \sum_{a=1}^{N_E^V} \mathbf{x}(\mathbf{x}_a), \quad (7)$$

and  $\bar{u}_1$  and  $\bar{u}_2$  are the components of the mean of the values that the displacement  $\mathbf{u}$  takes over the vertices of the element; i.e.,

$$\bar{\mathbf{u}} = \begin{bmatrix} \bar{u}_1 \\ \bar{u}_2 \end{bmatrix} = \frac{1}{N_E^V} \sum_{a=1}^{N_E^V} \mathbf{u}(\mathbf{x}_a). \quad (8)$$

In other words,  $\bar{\mathbf{x}}$  and  $\bar{\mathbf{u}}$  represents the geometric center of the element and its associated displacement vector, respectively; the terms  $\hat{\varepsilon}_{ij}$  are components of the element average  $\hat{\boldsymbol{\varepsilon}} = \frac{1}{|E|} \int_E \boldsymbol{\varepsilon} d\mathbf{x}$ , and  $\hat{\omega}_{12}$  is the component of the element average  $\hat{\boldsymbol{\omega}} = \frac{1}{|E|} \int_E \boldsymbol{\omega} d\mathbf{x}$ , where  $\boldsymbol{\omega}$  is the skew-symmetric tensor that represents rotations. These element averages are evaluated on the boundary of  $E$  by invoking the divergence theorem, which gives the following identities:

$$\hat{\boldsymbol{\varepsilon}}(\mathbf{u}_h) = \frac{1}{|E|} \int_E \boldsymbol{\varepsilon}(\mathbf{u}_h) d\mathbf{x} = \frac{1}{2|E|} \int_{\partial E} (\mathbf{u}_h \otimes \mathbf{n} + \mathbf{n} \otimes \mathbf{u}_h) ds, \quad (9)$$

$$\hat{\boldsymbol{\omega}}(\mathbf{u}_h) = \frac{1}{|E|} \int_E \boldsymbol{\omega}(\mathbf{u}_h) d\mathbf{x} = \frac{1}{2|E|} \int_{\partial E} (\mathbf{u}_h \otimes \mathbf{n} - \mathbf{n} \otimes \mathbf{u}_h) ds. \quad (10)$$

### 3.2. Discretization of field variables

Following a Galerkin approach, the element trial and test functions,  $\mathbf{u}_h$  and  $\mathbf{v}_h$ , respectively, are assumed to be discretized as

$$\mathbf{u}_h = \begin{bmatrix} u_{1h} \\ u_{2h} \end{bmatrix} = \sum_{a=1}^{N_E^V} \phi_a(\mathbf{x}) \mathbf{u}_a, \quad \mathbf{v}_h = \begin{bmatrix} v_{1h} \\ v_{2h} \end{bmatrix} = \sum_{a=1}^{N_E^V} \phi_a(\mathbf{x}) \mathbf{v}_a, \quad (11)$$

where  $\{\phi_a(\mathbf{x})\}_{a=1}^{N_E^V}$  are basis functions that form a partition of unity. Eqs. (8)–(10) reveal that all what is needed regarding the basis functions is the knowledge of their behavior on the element boundary. Thus, in the linear VEM the following behavior for the basis functions is assumed on the element boundary:

- basis functions are piecewise linear (edge by edge);
- basis functions are continuous on the element edges.

This means that the basis functions possess the Kronecker-delta property on the element edges, and hence they behave like the one-dimensional hat function.

When establishing the element matrices, we will see that these matrices are written in terms of the basis functions on the element boundary through (9) and the discretization of the displacements using (11). The element matrices will be then computed algebraically using the above assumptions in such a way that the basis functions are never computed. Thus, it is stressed that in the VEM the basis functions are not (and do not need to be) known explicitly.

### 3.3. VEM bilinear form

The projection operator (6) is derived<sup>2</sup> from the following orthogonality condition at the element level:

$$a_E(\mathbf{u}_h - \Pi \mathbf{u}_h, \mathbf{p}) = a_E(\mathbf{p}, \mathbf{v}_h - \Pi \mathbf{v}_h) = 0 \quad \forall \mathbf{p} \in [\mathcal{P}(E)]^2, \quad (12)$$

where  $[\mathcal{P}(E)]^2$  is the space of linear displacements over the element. This orthogonality condition states that the nonpolynomial terms  $\mathbf{u}_h - \Pi \mathbf{u}_h$  in  $E$ , measured in the energy norm, are orthogonal

---

<sup>2</sup>The derivation is given in Ref. [21]



to  $[\mathcal{P}(E)]^2$ . Using the decomposition (5) along with condition (12), and noting that  $\Pi \mathbf{u}_h$  and  $\Pi \mathbf{v}_h \in [\mathcal{P}(E)]^2$ , the following VEM representation of the bilinear form is obtained:

$$a_E(\mathbf{u}_h, \mathbf{v}_h) = a_E(\Pi \mathbf{u}_h, \Pi \mathbf{v}_h) + a_E(\mathbf{u}_h - \Pi \mathbf{u}_h, \mathbf{v}_h - \Pi \mathbf{v}_h). \quad (13)$$

The VEM bilinear form can be further elaborated. For convenience, the projection operator (6) is rewritten as

$$\Pi \mathbf{u}_h = \mathbf{h}(\mathbf{x}) \widehat{\boldsymbol{\varepsilon}}(\mathbf{u}_h) + \mathbf{g}(\mathbf{x}) \mathbf{r}(\mathbf{u}_h), \quad (14)$$

where

$$\mathbf{h}(\mathbf{x}) = \begin{bmatrix} (x_1 - \bar{x}_1) & 0 & \frac{1}{2}(x_2 - \bar{x}_2) \\ 0 & (x_2 - \bar{x}_2) & \frac{1}{2}(x_1 - \bar{x}_1) \end{bmatrix}, \quad \mathbf{g}(\mathbf{x}) = \begin{bmatrix} 1 & 0 & \frac{1}{2}(x_2 - \bar{x}_2) \\ 0 & 1 & -\frac{1}{2}(x_1 - \bar{x}_1) \end{bmatrix}, \quad (15)$$

$$\mathbf{r}(\mathbf{u}_h) = \begin{bmatrix} \bar{u}_1 & \bar{u}_2 & 2\widehat{\omega}_{12} \end{bmatrix}^\top, \quad (16)$$

and

$$\widehat{\boldsymbol{\varepsilon}}(\mathbf{u}_h) = \begin{bmatrix} \widehat{\varepsilon}_{11} & \widehat{\varepsilon}_{22} & 2\widehat{\varepsilon}_{12} \end{bmatrix}^\top \quad (17)$$

is the vector form of the element average strain. From now on, we always use this vector form when referring to the element average strain  $\widehat{\boldsymbol{\varepsilon}}$ .

Using the bilinear form written in terms of the vector form of the strain — that is,  $a(\mathbf{u}_h, \mathbf{v}_h) = \int_{\Omega} \boldsymbol{\varepsilon}^\top(\mathbf{v}_h) \mathbf{D} \boldsymbol{\varepsilon}(\mathbf{u}_h)$ , where  $\mathbf{D}$  is the constitutive matrix — and noting that  $\mathbf{r}(\mathbf{u}_h)$  represents rigid body translations and rotation, and that these do not produce strain energy, the first term on the right-hand side of (13) can be written, as follows:

$$\begin{aligned} a_E(\Pi \mathbf{u}_h, \Pi \mathbf{v}_h) &= \int_E \left[ \frac{\partial \Pi v_{1h}}{\partial x_1} \quad \frac{\partial \Pi v_{2h}}{\partial x_2} \quad \frac{\partial \Pi v_{1h}}{\partial x_2} + \frac{\partial \Pi v_{2h}}{\partial x_1} \right] \mathbf{D} \begin{bmatrix} \frac{\partial \Pi u_{1h}}{\partial x_1} \\ \frac{\partial \Pi u_{2h}}{\partial x_2} \\ \frac{\partial \Pi u_{1h}}{\partial x_2} + \frac{\partial \Pi u_{2h}}{\partial x_1} \end{bmatrix} d\mathbf{x} \\ &= \int_E \widehat{\boldsymbol{\varepsilon}}^\top(\mathbf{v}_h) \mathbf{D} \widehat{\boldsymbol{\varepsilon}}(\mathbf{u}_h) d\mathbf{x}. \end{aligned} \quad (18)$$

For an isotropic linear elastic material, the constitutive matrix is given by

$$\mathbf{D} = \frac{E_Y}{(1 + \nu)(1 - 2\nu)} \begin{bmatrix} 1 - \nu & \nu & 0 \\ \nu & 1 - \nu & 0 \\ 0 & 0 & \frac{1-2\nu}{2} \end{bmatrix} \quad (19)$$

for plane strain condition, and

$$\mathbf{D} = \frac{E_Y}{1 - \nu^2} \begin{bmatrix} 1 & \nu & 0 \\ \nu & 1 & 0 \\ 0 & 0 & \frac{1-\nu}{2} \end{bmatrix} \quad (20)$$

for plane stress condition, where  $E_Y$  is the Young's modulus and  $\nu$  is the Poisson's ratio.

The second term on the right-hand side of (13) can be written as

$$a_E(\mathbf{u}_h - \Pi\mathbf{u}_h, \mathbf{v}_h - \Pi\mathbf{v}_h) = (\mathbf{1} - \Pi)^\top a_E(\mathbf{v}_h, \mathbf{u}_h)(\mathbf{1} - \Pi), \quad (21)$$

which reveals that  $a_E(\mathbf{u}_h - \Pi\mathbf{u}_h, \mathbf{v}_h - \Pi\mathbf{v}_h)$  is not computable since  $a_E(\mathbf{v}_h, \mathbf{u}_h)$  would need to be evaluated inside the element using cubature, but the VEM basis functions are not known inside the element. However, since  $a_E(\mathbf{u}_h - \Pi\mathbf{u}_h, \mathbf{v}_h - \Pi\mathbf{v}_h)$  is meant to only provide stability,  $a_E(\mathbf{v}_h, \mathbf{u}_h)$  can be conveniently approximated by a bilinear form  $s_E(\cdot, \cdot)$  that is computable while preserving the coercivity of the system. In other words,  $s_E(\mathbf{v}_h, \mathbf{u}_h)$  must be positive definite and scale like  $a_E(\cdot, \cdot)$  in the kernel of  $\Pi$  [52, 53].

Using (18) and (21) with the approximation  $a_E(\mathbf{v}_h, \mathbf{u}_h) = s_E(\mathbf{v}_h, \mathbf{u}_h)$ , the VEM bilinear form for plane elasticity is written as

$$a_{h,E}(\mathbf{u}_h, \mathbf{v}_h) = \int_E \hat{\boldsymbol{\varepsilon}}^\top(\mathbf{v}_h) \mathbf{D} \hat{\boldsymbol{\varepsilon}}(\mathbf{u}_h) d\mathbf{x} + (\mathbf{1} - \Pi)^\top s_E(\mathbf{v}_h, \mathbf{u}_h)(\mathbf{1} - \Pi) \quad (22)$$

### 3.4. VEM element stiffness matrix

The discrete element average strain is computed using (11), as follows:

$$\widehat{\boldsymbol{\varepsilon}}_h(\mathbf{u}_h) = \widehat{\boldsymbol{\varepsilon}} \left( \sum_{a=1}^{N_E^V} \phi_a(\mathbf{x}) \mathbf{u}_a \right) = \mathbf{B} \mathbf{d}, \quad (23)$$

where

$$\mathbf{d} = \left[ u_{11} \ u_{21} \ \cdots \ u_{1a} \ u_{2a} \ \cdots \ u_{1N_E^V} \ u_{2N_E^V} \right]^T \quad (24)$$

is the column vector of element nodal displacements and

$$\mathbf{B} = \left[ \mathbf{B}_1 \ \cdots \ \mathbf{B}_a \ \cdots \ \mathbf{B}_{N_E^V} \right], \quad \mathbf{B}_a = \begin{bmatrix} q_{1a} & 0 \\ 0 & q_{2a} \\ q_{2a} & q_{1a} \end{bmatrix}, \quad (25)$$

where  $q_{ia} = \frac{1}{|E|} \int_{\partial E} \phi_a(\mathbf{x}) n_i ds$ . Since the VEM basis functions are assumed to be piecewise linear (edge by edge) and continuous on the element boundary,  $q_{ia}$  can be exactly computed using a trapezoidal rule, which gives the following algebraic expression:

$$q_{ia} = \frac{1}{2|E|} (|e_{a-1}| n_{i(a-1)} + |e_a| n_{ia}), \quad i = 1, 2, \quad (26)$$

where  $n_{ia}$  is the  $i$ -th component of  $\mathbf{n}_a$  and  $|e_a|$  is the length of the edge incident to node  $a$  as defined in Fig. 1. Using (23) and noting that  $\widehat{\boldsymbol{\varepsilon}}$  and  $\mathbf{D}$  are constant over the element, the discrete version of the first term on the right-hand side of (22) is written as

$$\int_E \widehat{\boldsymbol{\varepsilon}}_h^T(\mathbf{v}_h) \mathbf{D} \widehat{\boldsymbol{\varepsilon}}_h(\mathbf{u}_h) d\mathbf{x} = |E| \widehat{\boldsymbol{\varepsilon}}_h^T(\mathbf{v}_h) \mathbf{D} \widehat{\boldsymbol{\varepsilon}}_h(\mathbf{u}_h) = \mathbf{q}^T \left( |E| \mathbf{B}^T \mathbf{D} \mathbf{B} \right) \mathbf{d}, \quad (27)$$

where  $\mathbf{q}$  is a column vector similar to (24) that contains the element nodal values associated with  $\mathbf{v}_h$ .

To obtain the discrete version of the second term on the right-hand side of (22), the discretization of  $\Pi$  is required. This demands the discretization of  $h(\mathbf{x})$ ,  $\widehat{\boldsymbol{\varepsilon}}(\mathbf{u}_h)$ ,  $g(\mathbf{x})$  and  $r(\mathbf{u}_h)$ . The

discretization of  $\widehat{\boldsymbol{\varepsilon}}(\mathbf{u}_h)$  is given in (23). The remainder terms are discretized, as follows:

$$\mathbf{h}_h(\mathbf{x}) = \sum_{a=1}^{N_E^V} \phi_a(\mathbf{x}) \mathbf{h}(\mathbf{x}_a) = \mathbf{N}\mathbf{H}, \quad (28)$$

$$\mathbf{g}_h(\mathbf{x}) = \sum_{a=1}^{N_E^V} \phi_a(\mathbf{x}) \mathbf{g}(\mathbf{x}_a) = \mathbf{N}\mathbf{G}, \quad (29)$$

$$\mathbf{r}_h = \mathbf{r} \left( \sum_{a=1}^{N_E^V} \phi_a(\mathbf{x}) \mathbf{u}_a \right) = \mathbf{R}\mathbf{d}, \quad (30)$$

where

$$\mathbf{N} = \left[ \mathbf{N}_1 \quad \cdots \quad \mathbf{N}_a \quad \cdots \quad \mathbf{N}_{N_E^V} \right], \quad \mathbf{N}_a = \begin{bmatrix} \phi_a(\mathbf{x}) & 0 \\ 0 & \phi_a(\mathbf{x}) \end{bmatrix}, \quad (31)$$

$$\mathbf{H} = \begin{bmatrix} \mathbf{H}_1 \\ \vdots \\ \mathbf{H}_a \\ \vdots \\ \mathbf{H}_{N_E^V} \end{bmatrix}, \quad \mathbf{H}_a = \begin{bmatrix} (x_{1a} - \bar{x}_1) & 0 & \frac{1}{2}(x_{2a} - \bar{x}_2) \\ 0 & (x_{2a} - \bar{x}_2) & \frac{1}{2}(x_{1a} - \bar{x}_1) \end{bmatrix}, \quad (32)$$

$$\mathbf{G} = \begin{bmatrix} \mathbf{G}_1 \\ \vdots \\ \mathbf{G}_a \\ \vdots \\ \mathbf{G}_{N_E^V} \end{bmatrix}, \quad \mathbf{G}_a = \begin{bmatrix} 1 & 0 & \frac{1}{2}(x_{2a} - \bar{x}_2) \\ 0 & 1 & -\frac{1}{2}(x_{1a} - \bar{x}_1) \end{bmatrix}, \quad (33)$$

and

$$\mathbf{R} = \left[ \mathbf{R}_1 \quad \cdots \quad \mathbf{R}_a \quad \cdots \quad \mathbf{R}_{N_E^V} \right], \quad \mathbf{R}_a = \begin{bmatrix} \frac{1}{N_E^V} & 0 \\ 0 & \frac{1}{N_E^V} \\ q_{2a} & -q_{1a} \end{bmatrix}. \quad (34)$$

Therefore, the discrete  $\Pi$  can be written as

$$\Pi_h \mathbf{u}_h = \mathbf{NHBd} + \mathbf{NGRd} = \mathbf{N}(\mathbf{HB} + \mathbf{GR})\mathbf{d}, \quad (35)$$

which defines the projection matrix as

$$\mathbf{P} = \mathbf{HB} + \mathbf{GR}. \quad (36)$$

Using the projection matrix and the discrete field  $\mathbf{u}_h = \sum_{a=1}^{N_E^V} \phi_a(\mathbf{x})\mathbf{u}_a = \mathbf{Nd}$ , the discrete version of the second term on the right-hand side of (22) is

$$\mathbf{q}^\top (\mathbf{I} - \mathbf{P})^\top s_E(\mathbf{N}^\top, \mathbf{N})(\mathbf{I} - \mathbf{P})\mathbf{d} = \mathbf{q}^\top (\mathbf{I} - \mathbf{P})^\top \mathbf{S} (\mathbf{I} - \mathbf{P})\mathbf{d}. \quad (37)$$

Finally, using (27) and (37), the discrete VEM bilinear form is written as

$$a_{h,E}(\mathbf{u}_h, \mathbf{v}_h) = \mathbf{q}^\top \left\{ |E| \mathbf{B}^\top \mathbf{D} \mathbf{B} + (\mathbf{I} - \mathbf{P})^\top \mathbf{S} (\mathbf{I} - \mathbf{P}) \right\} \mathbf{d}, \quad (38)$$

which defines the element stiffness matrix as the sum of the element consistency stiffness matrix,  $\mathbf{K}_E^c$ , and the element stability stiffness matrix,  $\mathbf{K}_E^s$ , as follows:

$$\mathbf{K}_E = \mathbf{K}_E^c + \mathbf{K}_E^s, \quad \mathbf{K}_E^c = |E| \mathbf{B}^\top \mathbf{D} \mathbf{B}, \quad \mathbf{K}_E^s = (\mathbf{I} - \mathbf{P})^\top \mathbf{S} (\mathbf{I} - \mathbf{P}). \quad (39)$$

### 3.5. VEM element force vector

For linear fields, the VEM version of the loading term in the weak form (2) is computed at the element level, as follows [44, 52, 55]:

$$\ell_E^b(\mathbf{v}_h) = \int_E \widehat{\mathbf{b}} \cdot \bar{\mathbf{v}}_h \, d\mathbf{x} = |E| \widehat{\mathbf{b}} \cdot \bar{\mathbf{v}}_h, \quad \widehat{\mathbf{b}} = \frac{1}{|E|} \int_E \mathbf{b} \, d\mathbf{x}, \quad \bar{\mathbf{v}}_h = \frac{1}{N_E^V} \sum_{a=1}^{N_E^V} \mathbf{v}_a \quad (40)$$

for the loading term associated with the body forces, and similarly

$$\ell_e^t(\mathbf{v}_h) = |e| \widehat{\mathbf{t}}_N \cdot \bar{\mathbf{v}}_h, \quad \widehat{\mathbf{t}}_N = \frac{1}{|e|} \int_e \mathbf{t}_N ds, \quad \bar{\mathbf{v}}_h = \frac{1}{N_e^V} \sum_{a=1}^{N_e^V} \mathbf{v}_a \quad (41)$$

for the loading term associated with the tractions applied on an edge located on the Neumann boundary, where  $e$  and  $|e|$  are as defined in Fig. 1 and  $N_e^V$  is the number of nodes of the edge. The discrete versions of these loading terms are  $\ell_{h,E}^b(\mathbf{v}_h) = \mathbf{q}^\top \mathbf{f}_E^b$  and  $\ell_{h,e}^t(\mathbf{v}_h) = \mathbf{q}^\top \mathbf{f}_e^t$ , where  $\mathbf{f}_E^b$  and  $\mathbf{f}_e^t$  are the element force vectors given, respectively, by

$$\mathbf{f}_E^b = |E| \bar{\mathbf{N}}^\top \widehat{\mathbf{b}}, \quad (42)$$

where

$$\bar{\mathbf{N}} = \left[ \bar{\mathbf{N}}_1 \quad \cdots \quad \bar{\mathbf{N}}_a \quad \cdots \quad \bar{\mathbf{N}}_{N_E^V} \right], \quad \bar{\mathbf{N}}_a = \begin{bmatrix} \frac{1}{N_E^V} & 0 \\ 0 & \frac{1}{N_E^V} \end{bmatrix}, \quad (43)$$

and

$$\mathbf{f}_e^t = |e| \bar{\mathbf{N}}_\Gamma^\top \widehat{\mathbf{t}}_N, \quad (44)$$

where

$$\bar{\mathbf{N}}_\Gamma = \begin{bmatrix} \frac{1}{N_e^V} & 0 & \frac{1}{N_e^V} & 0 \\ 0 & \frac{1}{N_e^V} & 0 & \frac{1}{N_e^V} \end{bmatrix} = \begin{bmatrix} \frac{1}{2} & 0 & \frac{1}{2} & 0 \\ 0 & \frac{1}{2} & 0 & \frac{1}{2} \end{bmatrix} \quad (45)$$

since the number of nodes of an edge is  $N_e^V = 2$ .

#### 4. Node-based uniform strain virtual elements (NVEM)

The virtual element method for plane elasticity described in Section 3 is prone to volumetric locking in the limit  $\nu \rightarrow 0.5$ . We propose to use a nodal averaging operator  $\pi_I$  in (13) that is designed to preclude volumetric locking without introducing additional degrees of freedom. This nodal averaging operator leads to a nodal version of the VEM bilinear form, as follows:

$$a_{h,I}(\mathbf{u}_h, \mathbf{v}_h) = a_I(\pi_I[II\mathbf{u}_h], \pi_I[II\mathbf{v}_h]) + s_I(\pi_I[\mathbf{u}_h - II\mathbf{u}_h], \pi_I[\mathbf{v}_h - II\mathbf{v}_h]), \quad (46)$$

where according to the VEM theory,  $s_I(\pi_I[\mathbf{u}_h - \Pi\mathbf{u}_h], \pi_I[\mathbf{v}_h - \Pi\mathbf{v}_h])$  is a computable approximation to  $a_I(\pi_I[\mathbf{u}_h - \Pi\mathbf{u}_h], \pi_I[\mathbf{v}_h - \Pi\mathbf{v}_h])$  and is meant to provide stability.

#### 4.1. Construction of the nodal averaging operator

Each node of the mesh is associated with their own patch of virtual elements. The patch for node  $I$  is denoted by  $\mathcal{T}_I$  and is defined as the set of virtual elements connected to node  $I$  (see Fig. 2). Each node of a virtual element  $E$  in the patch is assigned the area  $\frac{1}{N_E}|E|$ ; that is, the area of an element is uniformly distributed among its nodes. The representative area of node  $I$  is denoted by  $|I|$  and is computed by addition of all the areas that are assigned to node  $I$  from the elements in  $\mathcal{T}_I$ ; that is,

$$|I| = \sum_{E \in \mathcal{T}_I} \frac{1}{N_E}|E|. \quad (47)$$

Similarly, each node of a virtual element  $E$  is uniformly assigned the strain  $\frac{1}{N_E}\widehat{\boldsymbol{\varepsilon}}(\mathbf{u}_h)$ . On considering each strain assigned to node  $I$  from the elements in  $\mathcal{T}_I$ , we define the *node-based uniform strain*, as follows:

$$\boldsymbol{\varepsilon}_I(\mathbf{u}_h) = \frac{1}{|I|} \sum_{E \in \mathcal{T}_I} |E| \frac{1}{N_E} \widehat{\boldsymbol{\varepsilon}}(\mathbf{u}_h). \quad (48)$$

Since  $\widehat{\boldsymbol{\varepsilon}}(\mathbf{u}_h)$  is by definition given at the element level, then from Eq. (48) the following nodal averaging operator is proposed:

$$\pi_I[\cdot] = \frac{1}{|I|} \sum_{E \in \mathcal{T}_I} |E| \frac{1}{N_E} [\cdot]_E, \quad (49)$$

where  $[\cdot]_E$  denotes evaluation over the element  $E$ . Using this nodal averaging operator, the nodal representation of a function  $F$  is obtained as

$$F_I = \pi_I[F] = \frac{1}{|I|} \sum_{E \in \mathcal{T}_I} |E| \frac{1}{N_E} [F]_E. \quad (50)$$

The idea of having a nodal strain (like the one in (48)) that is representative of the nodal patch  $\mathcal{T}_I$  has long been used in meshfree and finite element nodal integration techniques [11, 17, 29–33, 35, 36, 56]. In particular, the node-based uniform strain approach was developed for three-

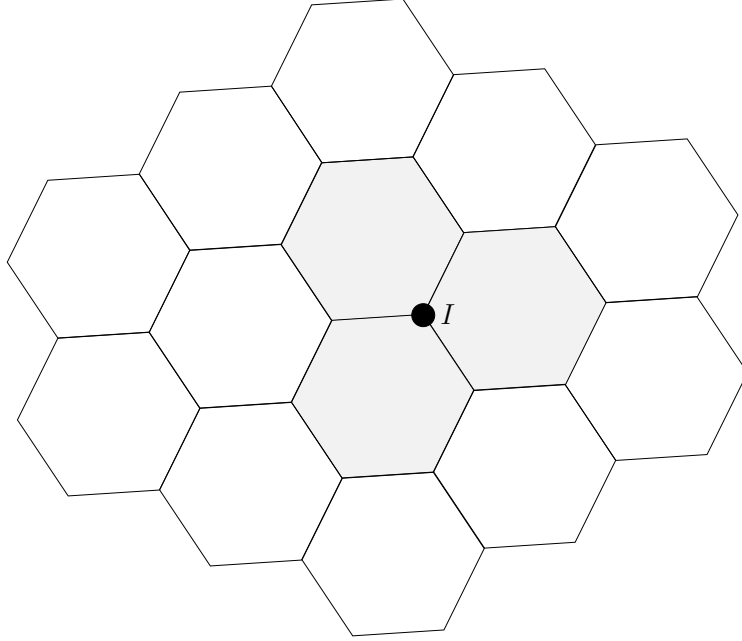


Fig. 2: Nodal patch  $\mathcal{T}_I$  (shaded elements) formed by the virtual elements that are connected to node  $I$ .

node triangular and four-node tetrahedral elements in Ref. [30], and proved to perform well for nearly incompressible solids. However, that approach presented stability issues in some particular instances and required stabilization [11]. Within the VEM framework, stabilization is obtained by construction of the method, and hence in combining the node-based uniform strain approach with the VEM, no stability issues will arise.

#### 4.2. NVEM bilinear form

Using the nodal averaging operator (49), the nodal representation of the VEM bilinear form for plane elasticity (Eq. (22)) is written as

$$a_{h,I}(\mathbf{u}_h, \mathbf{v}_h) = |I| \boldsymbol{\varepsilon}_I^\top(\mathbf{v}_h) \mathbf{D} \boldsymbol{\varepsilon}_I(\mathbf{u}_h) + (\mathbf{1} - \Pi)_I^\top s_I(\mathbf{v}_h, \mathbf{u}_h) (\mathbf{1} - \Pi)_I. \quad (51)$$

Let  $N$  be the total number of nodes in the mesh. The global bilinear form is obtained by summing through the  $N$  nodes, as follows:

$$a_h(\mathbf{u}_h, \mathbf{v}_h) = \sum_{I=1}^N \left[ |I| \boldsymbol{\varepsilon}_I^\top(\mathbf{v}_h) \mathbf{D} \boldsymbol{\varepsilon}_I(\mathbf{u}_h) + (\mathbf{1} - \Pi)_I^\top s_I(\mathbf{v}_h, \mathbf{u}_h) (\mathbf{1} - \Pi)_I \right]. \quad (52)$$



#### 4.3. NVEM nodal stiffness matrix

The nodal stiffness matrix that arises from (51) is the nodal version of (39). This gives

$$\mathbf{K}_I = \mathbf{K}_I^c + \mathbf{K}_I^s, \quad \mathbf{K}_I^c = |I| \mathbf{B}_I^\top \mathbf{D} \mathbf{B}_I, \quad \mathbf{K}_I^s = (\mathbf{I} - \mathbf{P})_I^\top \mathbf{S}_I (\mathbf{I} - \mathbf{P})_I, \quad (53)$$

where  $\mathbf{B}_I = \pi_I[\mathbf{B}]$ ,  $(\mathbf{I} - \mathbf{P})_I = \pi_I[\mathbf{I} - \mathbf{P}]$ , and  $\mathbf{S}_I$  is defined in Section 5.

#### 4.4. NVEM nodal force vector

The nodal force vector associated with the body forces is the nodal representation of (42) and is given by

$$\mathbf{f}_I^b = |I| \bar{\mathbf{N}}_I^\top \hat{\mathbf{b}}_I, \quad (54)$$

where  $\bar{\mathbf{N}}_I = \pi_I[\bar{\mathbf{N}}]$  and  $\hat{\mathbf{b}}_I = \pi_I[\hat{\mathbf{b}}]$ . Similarly, the nodal force vector associated with the tractions is given by the nodal representation of (44), as follows:

$$\mathbf{f}_I^t = |I| \bar{\mathbf{N}}_{I,I}^\top \hat{\mathbf{t}}_{N,I}, \quad (55)$$

where the nodal components are now computed with respect to the one-dimensional domain on the Neumann boundary; that is,  $|I| = \sum_{e \in \mathcal{T}_I} \frac{1}{2} |e|$ , where  $e$  is an element's edge located on the Neumann boundary and  $|e|$  its length;  $\mathcal{T}_I$  now represents the set of edges connected to node  $I$  on the Neumann boundary. Proceeding as mentioned, the remainder nodal matrices are

$$\bar{\mathbf{N}}_{I,I} = \frac{1}{|I|} \sum_{e \in \mathcal{T}_I} |e| \frac{1}{2} [\bar{\mathbf{N}}_I]_e, \quad (56)$$

and

$$\hat{\mathbf{t}}_{N,I} = \frac{1}{|I|} \sum_{e \in \mathcal{T}_I} |e| \frac{1}{2} [\hat{\mathbf{t}}_N]_e. \quad (57)$$

### 5. Stabilization for node-based uniform strain virtual elements

Within the VEM framework, stabilization is one of the key ingredients to guarantee convergence. However, in nodal integration, stabilization can make the formulation somewhat stiff in the nearly

incompressible limit [17]. To mitigate this, a modified constitutive matrix  $\tilde{\mathbf{D}}$  can be used in lieu of the standard  $\mathbf{D}$  when computing the stability matrix. We opt for  $\tilde{\mathbf{D}}$  given as follows [11]:

$$\tilde{\mathbf{D}} = \mathbf{D}(\tilde{E}, \tilde{\nu}), \quad (58)$$

where

$$\tilde{E} = \frac{\tilde{\nu}(3\tilde{\lambda} + 2\tilde{\mu})}{\tilde{\lambda} + \tilde{\mu}}, \quad \tilde{\nu} = \frac{\tilde{\lambda}}{2(\tilde{\lambda} + \tilde{\mu})}; \quad (59)$$

$\tilde{\lambda}$  and  $\tilde{\mu}$  are, respectively, the modified Lamé's first and second parameters, which are calculated as follows:

$$\tilde{\mu} := \mu, \quad \tilde{\lambda} := \min(\lambda, 25\tilde{\mu}), \quad (60)$$

where  $\lambda$  and  $\mu$  are the Lamé parameters of the problem to solve. Similarly, another possibility to mitigate the stiff response is offered by the use of a modified constitutive matrix  $\mathbf{D}_\mu$  given by

$$\mathbf{D}_\mu = \begin{bmatrix} 2\mu & 0 & 0 \\ 0 & 2\mu & 0 \\ 0 & 0 & \mu \end{bmatrix}, \quad (61)$$

which omits the pressure parameter  $\lambda(\varepsilon_{11} + \varepsilon_{22})$  that is responsible of the possible stiff behavior. Alternatively, a simpler definition of  $\mathbf{D}_\mu$  that produces practically identical results is obtained by using the constitutive matrix that is related to the shear deformations; i.e.,

$$\mathbf{D}_\mu = \begin{bmatrix} 0 & 0 & 0 \\ 0 & 0 & 0 \\ 0 & 0 & \mu \end{bmatrix}. \quad (62)$$

We point out that the foregoing stabilization procedure with  $\mathbf{D}_\mu$  as given in (62) is similar to one of the stabilization approaches in the B-bar VEM [2] (see Appendix A therein).

Using the modified constitutive matrices, we define the stability matrix as the nodal version of the *D-recipe* stabilization technique [47, 57]. This gives two diagonal stability matrices whose

entries are given by

$$(\mathbf{S}_I)_{i,i} = \max\left(1, (|I| \mathbf{B}_I^\top \tilde{\mathbf{D}} \mathbf{B}_I)_{i,i}\right) \quad (63)$$

and

$$(\mathbf{S}_I)_{i,i} = \max\left(1, (|I| \mathbf{B}_I^\top \mathbf{D}_\mu \mathbf{B}_I)_{i,i}\right). \quad (64)$$

We refer to (63) and (64), respectively, as  $\tilde{\mathbf{D}}$  and  $\mathbf{D}_\mu$  stabilizations.

## 6. Numerical experiments

In this section, numerical experiments are conducted to demonstrate the accuracy, convergence and stability of the NVEM for compressible and nearly incompressible plane elasticity. The numerical results are compared with the B-bar VEM [2] and the standard linear VEM.

### 6.1. Colliding flow

We consider a simple model of colliding flow, which is a well-known and standard benchmark test problem (for example, see Refs. [58]) that can be solved using the linear elastostatic model with the following constitutive matrix:

$$\mathbf{D} = \begin{bmatrix} \lambda + 2\mu & \lambda & 0 \\ \lambda & \lambda + 2\mu & 0 \\ 0 & 0 & \mu \end{bmatrix},$$

where the Lamé parameters are set to  $\lambda = 5 \times 10^7$  and  $\mu = 1$ , which results in a Poisson's ratio  $\nu = 0.49999999$ . The problem is defined on the square domain  $\Omega = (0, 2)^2$  and possesses the following analytical solution [58]:

$$u_1 = 20(x_1 - 1)(x_2 - 1)^3 \quad (65a)$$

$$u_2 = 5(x_1 - 1)^4 - 5(x_2 - 1)^4 \quad (65b)$$

$$p = 60(x_1 - 1)^2(x_2 - 1) - 20(x_2 - 1)^3 \quad (65c)$$

Eqs. (65a) and (65b) are used as the Dirichlet boundary conditions along the boundary of the domain. The stabilizations presented in Section 5 are considered to assess the convergence of the method upon mesh refinement. A sample polygonal mesh used in the convergence study is shown in Fig. 3.

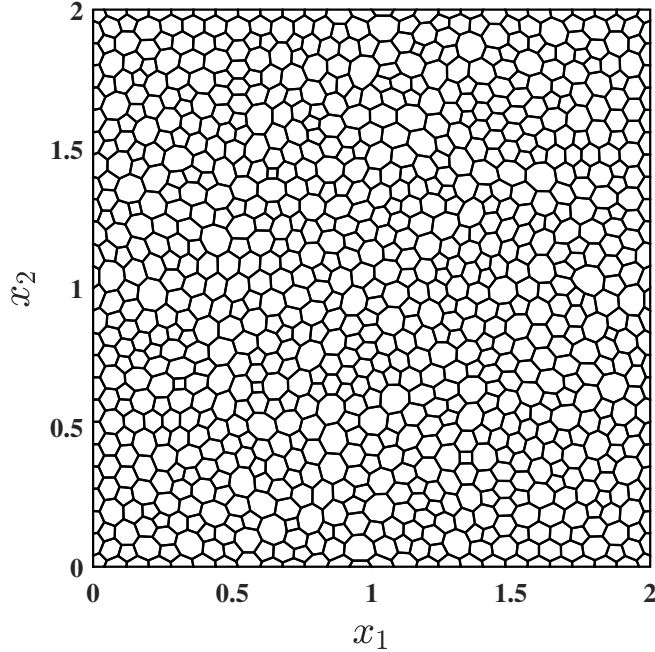


Fig. 3: Sample mesh for the colliding flow problem.

We start by showing the need for stability in the NVEM approach. Fig. 4 presents a comparison between unstabilized and stabilized solutions for the nodal fields  $\|\mathbf{u}_h\|$  and  $p_h$  — scatter plots are used for the NVEM as in this approach the field variables are known at the nodes. The unstabilized solutions exhibit marked spurious oscillations at the corners  $(0, 0)$  and  $(2, 0)$  (Figs. 4(a) and 4(c)), whereas the stabilized solutions become smooth on the whole domain (Figs. 4(b) and 4(d)).

The convergence and accuracy of the NVEM with  $\tilde{\mathbf{D}}$  and  $\mathbf{D}_\mu$  stabilizations are demonstrated in Fig. 5, where the  $L^2$  norm and the  $H^1$  seminorm of the displacement error, and the  $L^2$  norm of the pressure error indicate accurate solutions with optimal convergence rates of 2, 1 and 1, respectively. In comparison with the B-bar VEM approach, which is also accurate and optimally convergent, the NVEM approach is slightly more accurate in the  $H^1$  seminorm of the displacement

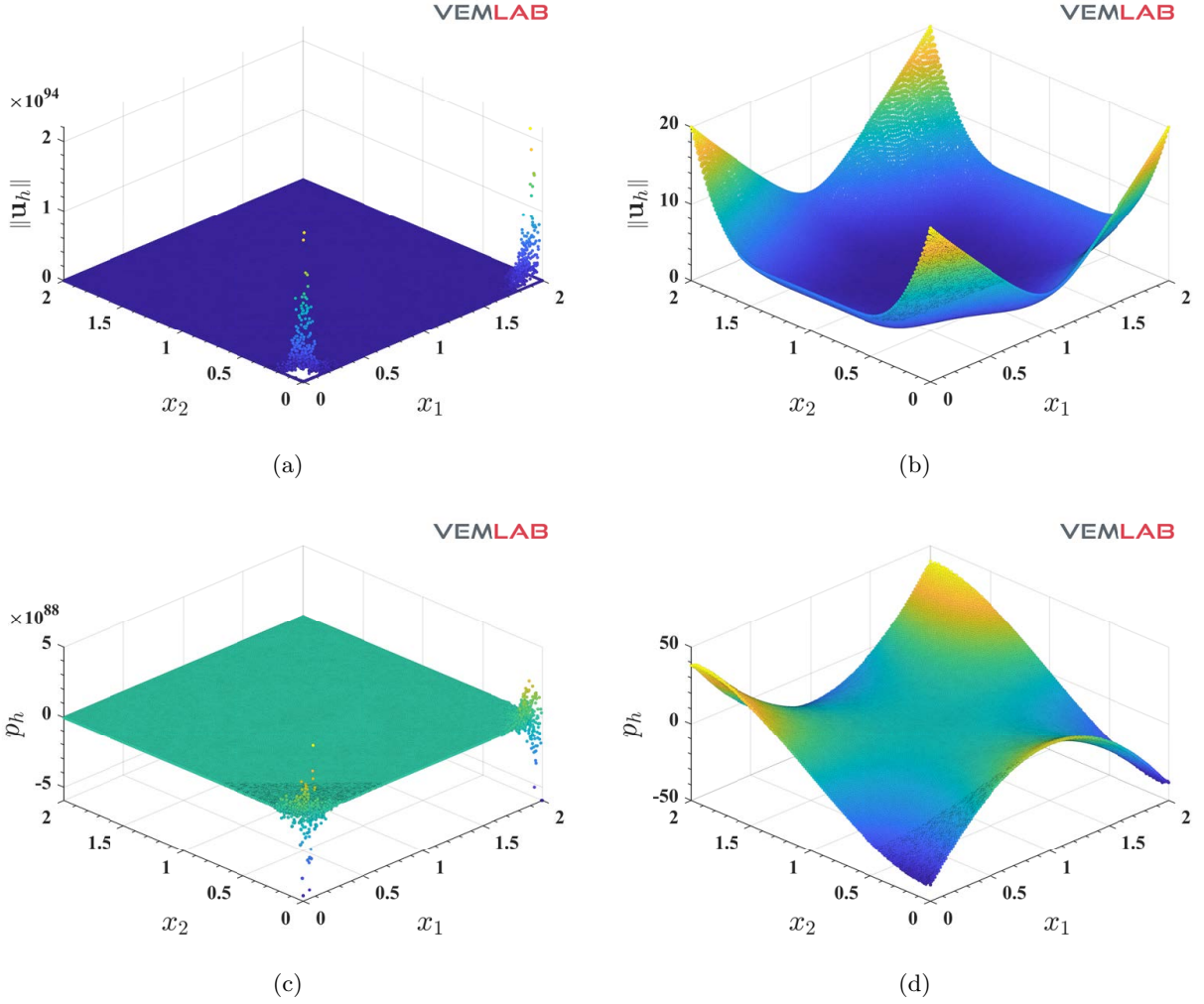


Fig. 4: Comparison between unstabilized and stabilized solutions in the NVEM for the colliding flow problem. (a) Unstabilized  $\|\mathbf{u}_h\|$ , (b) stabilized  $\|\mathbf{u}_h\|$ , (c) unstabilized  $\|p_h\|$  and (d) stabilized  $\|p_h\|$ .

error and the  $L^2$  norm of the pressure error. Finally, as expected, in these convergence plots the standard VEM solution behaves very inaccurate due to volumetric locking.

### 6.2. Cantilever beam subjected to a parabolic end load

A cantilever beam of unit thickness whose domain of analysis is  $\Omega = (0, 8) \times (-2, 2)$  is subjected to a parabolic end load  $P$  that is applied on the edge  $x = 8$ . The Dirichlet boundary conditions are applied on the edge  $x = 0$  according to the following exact solution given by Timoshenko and

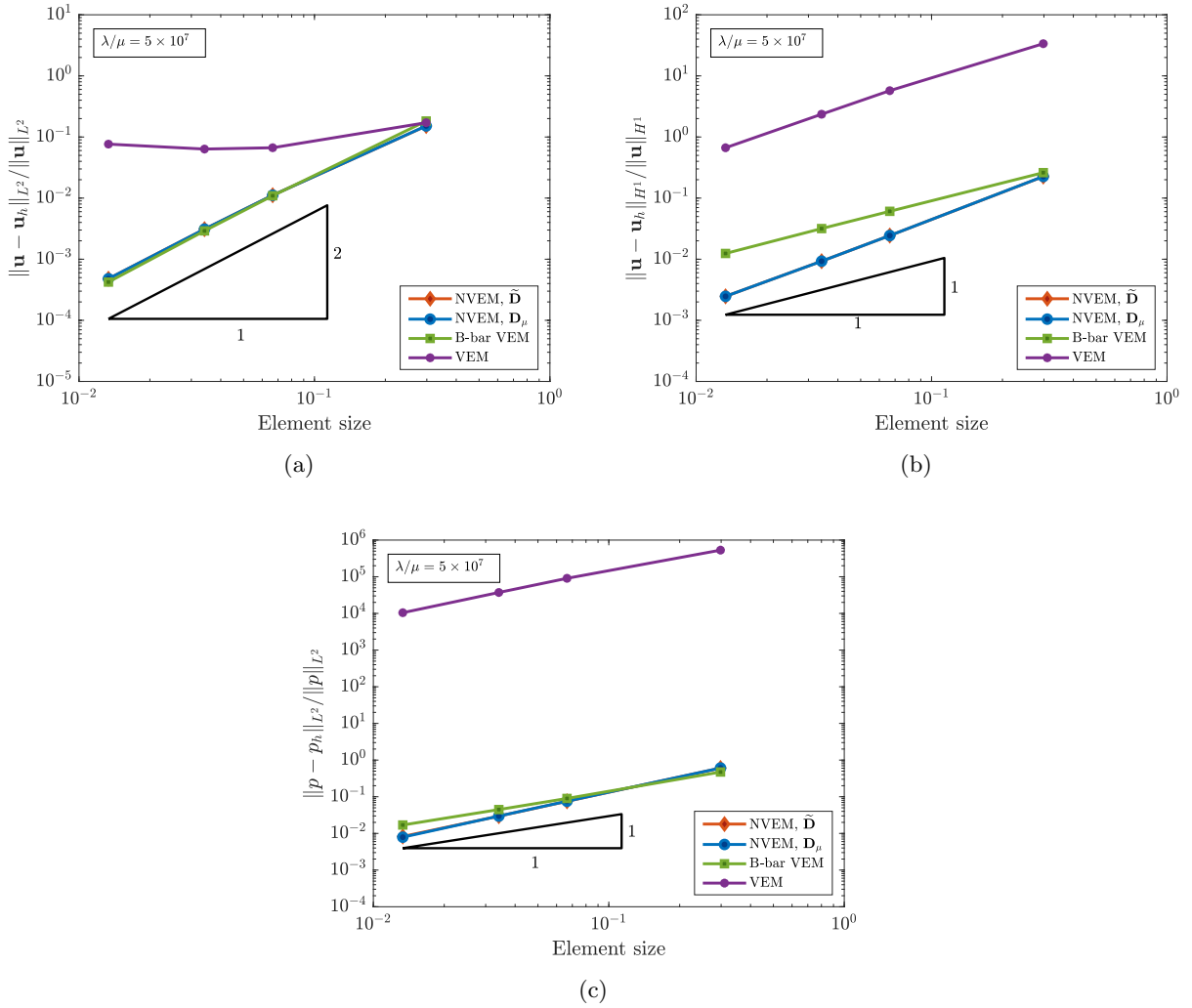


Fig. 5: Colliding flow problem. Convergence rates in the (a)  $L^2$  norm of the displacement error, (b)  $H^1$  seminorm of the displacement error and (c)  $L^2$  norm of the pressure error for the VEM, B-bar VEM and NVEM.

Goodier [59] for plane strain state:

$$u_1 = -\frac{Px_2}{6\bar{E}_Y I} \left( (6L - 3x_1)x_1 + (2 + \bar{\nu})x_2^2 - \frac{3D^2}{2}(1 + \bar{\nu}) \right),$$

$$u_2 = \frac{P}{6\bar{E}_Y I} (3\bar{\nu}x_2^2(L - x_1) + (3L - x_1)x_1^2)$$

with  $\bar{E}_Y = E_Y / (1 - \nu^2)$  and  $\bar{\nu} = \nu / (1 - \nu)$ , where  $E_Y$  and  $\nu$  are the Young's modulus and the Poisson's ratio of the linear elastic material, respectively;  $L$  is the length of the beam,  $D$  is the height of the beam, and  $I$  is the second-area moment of the beam section. The total load on

the Neumann boundary is  $P = -1000$ . The geometry and boundary conditions, and a sample polygonal mesh used in this study are shown in Fig. 6.

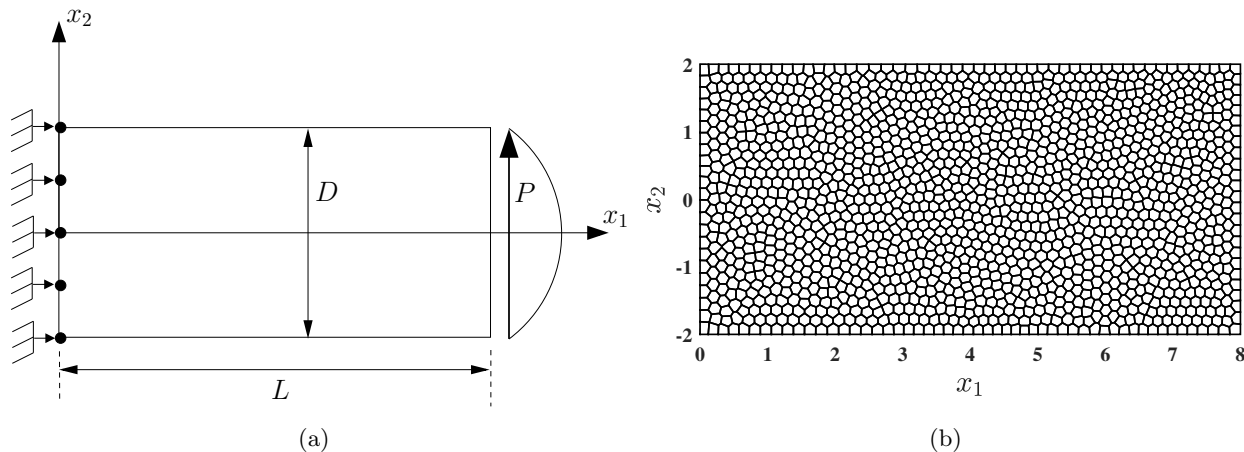


Fig. 6: Cantilever beam (a) geometry and boundary conditions, and (b) a sample mesh.

The convergence and accuracy of the NVEM is studied for two sets of material parameters. The first set is  $E = 10^7$  and  $\nu = 0.3$  (compressible elasticity), and the second set is  $E = 10^7$  and  $\nu = 0.499999$  (nearly incompressible elasticity).

### 6.2.1. Compressible elasticity

For compressible elasticity, Fig. 7 presents the  $L^2$  norm and the  $H^1$  seminorm of the displacement error, and the  $L^2$  norm of the pressure error, where it is observed that accurate solutions with optimal convergence rates of 2, 1 and 1, respectively, are delivered by the NVEM with  $\tilde{\mathbf{D}}$  and  $\mathbf{D}_\mu$  stabilizations. The VEM and the B-bar VEM also exhibit accurate solutions with optimal rates of convergence. In comparison with the VEM and the B-bar VEM, the NVEM is more accurate in the  $H^1$  seminorm of the displacement error and the  $L^2$  norm of the pressure error, whereas less accurate in the  $L^2$  norm of the displacement error.

### 6.2.2. Nearly incompressible elasticity

For nearly incompressible elasticity, the NVEM and the B-bar VEM are accurate and optimally convergent, as shown in Fig. 8. Like in the compressible case, the NVEM is more accurate than the B-bar VEM in the  $H^1$  seminorm of the displacement error and the  $L^2$  norm of the pressure

error, whereas less accurate in the  $L^2$  norm of the displacement error. As expected, Fig. 8 also exhibits very inaccurate solutions for the VEM due to volumetric locking.

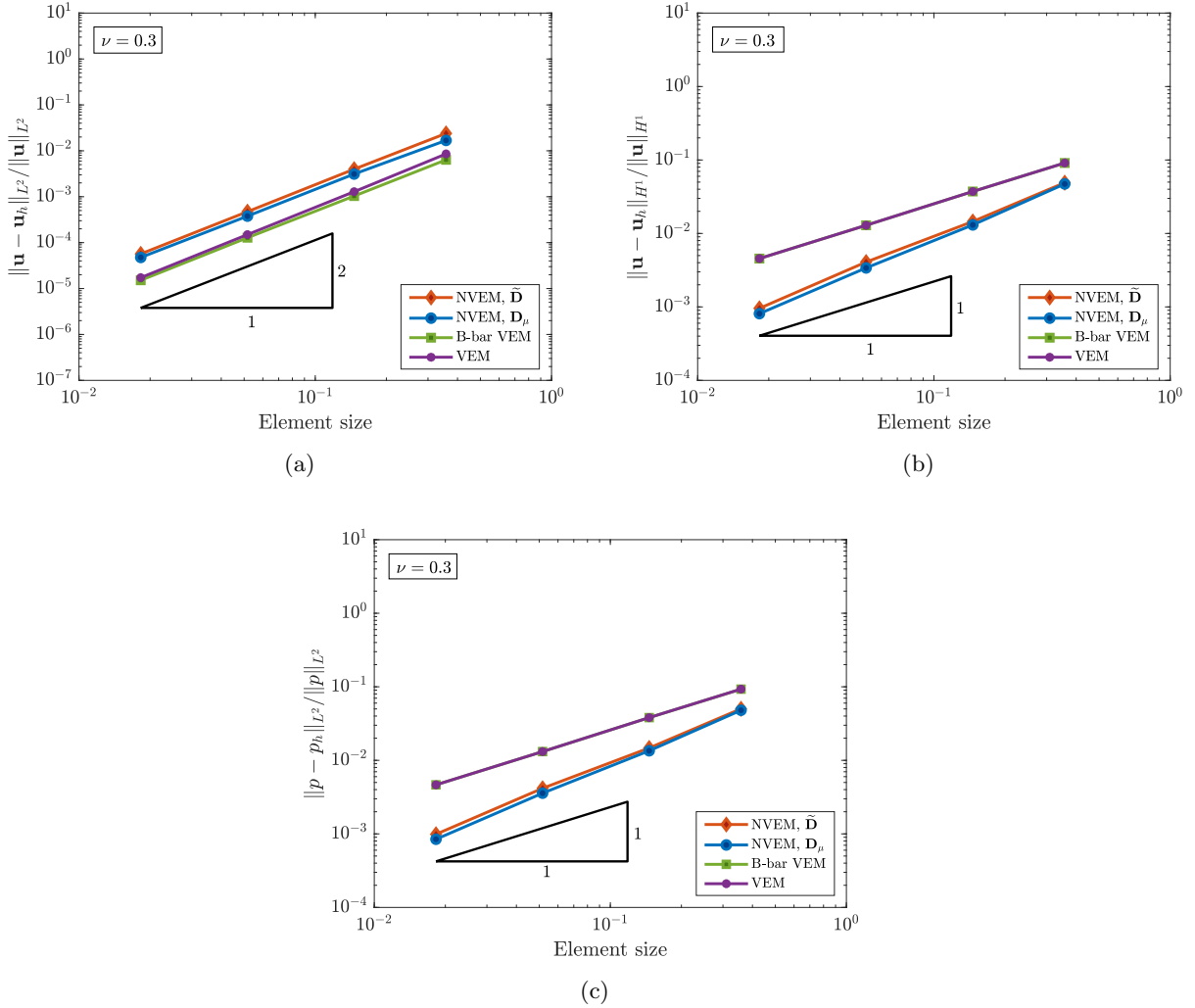


Fig. 7: Cantilever beam problem with material parameters  $E_Y = 10^7$  and  $\nu = 0.3$ . Convergence rates in the (a)  $L^2$  norm of the displacement error, (b)  $H^1$  seminorm of the displacement error and (c)  $L^2$  norm of the pressure error for the VEM, B-bar VEM and NVEM.

### 6.3. Cook's membrane

This standard benchmark problem is suitable to test the performance of numerical formulations for nearly incompressible solid materials under combined bending and shear. The geometry and boundary conditions for this problem are schematically shown in Fig. 9. There, the left edge is clamped and the right edge is subjected to a shear load  $F = 6.25$  per unit length (total shear load



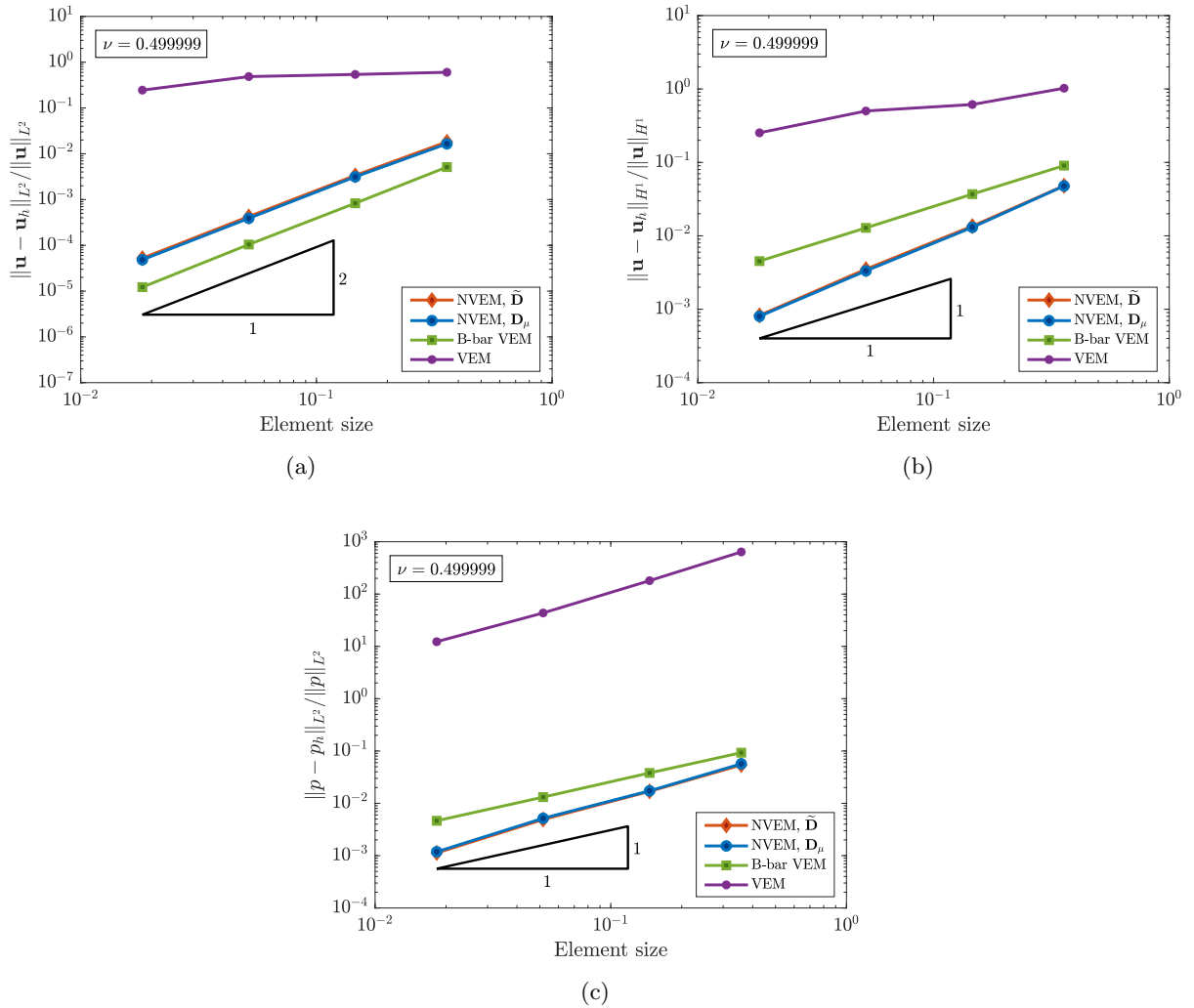


Fig. 8: Cantilever beam problem with material parameters  $E_Y = 10^7$  and  $\nu = 0.499999$ . Convergence rates in the (a)  $L^2$  norm of the displacement error, (b)  $H^1$  seminorm of the displacement error and (c)  $L^2$  norm of the pressure error for the VEM, B-bar VEM and NVEM.

of 100). The following material parameters are used:  $E = 250$  and  $\nu = 0.4999$ . In this example, a non standard mesh is tested. To this end, we define a master multielement region formed by five polygons, as shown in Fig. 10(a), where the center polygon is an eight-point star known as ‘Guñelve’. This master multielement is mapped into the membrane geometry several times to form the mesh. A sample ‘Guñelve’ mesh is shown in Fig. 10(b).

The convergence of the vertical tip displacement at point A upon mesh refinement is studied. For comparison purposes, a reference solution for the vertical tip displacement is found using a

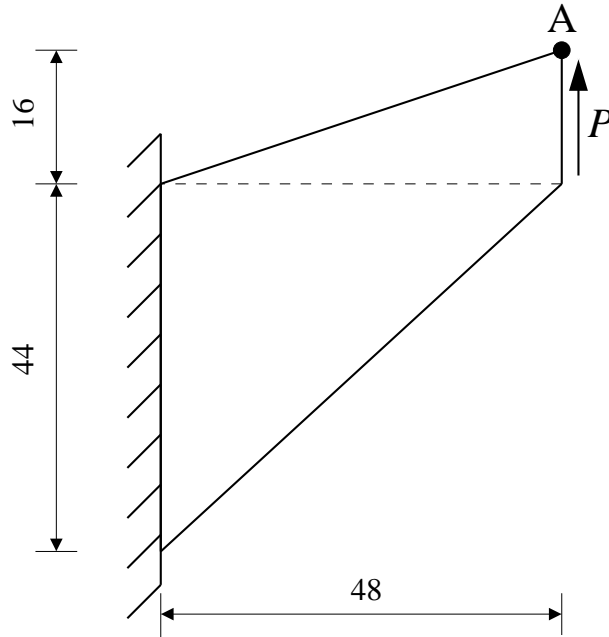


Fig. 9: Geometry and boundary conditions for the Cook's membrane problem.

highly refined mesh of eight-node quadrilateral finite elements. The result of this study is summarized in Fig. 11, where it is shown that the B-bar VEM and the NVEM solutions approach the reference value as the mesh is refined, and, as expected, the standard VEM exhibits very poor convergence due to volumetric locking.

Plots of the vertical displacement, pressure and von Mises stress fields are presented in Figs. 12, 13 and 14, respectively. Scatter plots are used for the NVEM as in this approach the field variables are known at the nodes. As expected, a very good agreement between the NVEM and the B-bar VEM solutions is observed in these plots.

#### 6.4. Infinite plate with a circular hole

This example is devoted to study an infinite plate with a circular hole that is loaded at infinity with the following tractions:  $\sigma_{11} = T$  and  $\sigma_{22} = \sigma_{12} = 0$  (see Fig. 15(a)). Due to the symmetry of the geometry and boundary conditions, a quarter of the domain is used as the domain of analysis (see Fig. 15(b)). Plane stress and plane strain conditions are considered. For plane stress condition, the material parameters are set to  $E_Y = 10^3$  and  $\nu = 0.3$  (compressible elasticity), and for plane strain condition, they are set to  $E_Y = 10^3$  and  $\nu = 0.499999$  (nearly incompressible elasticity).

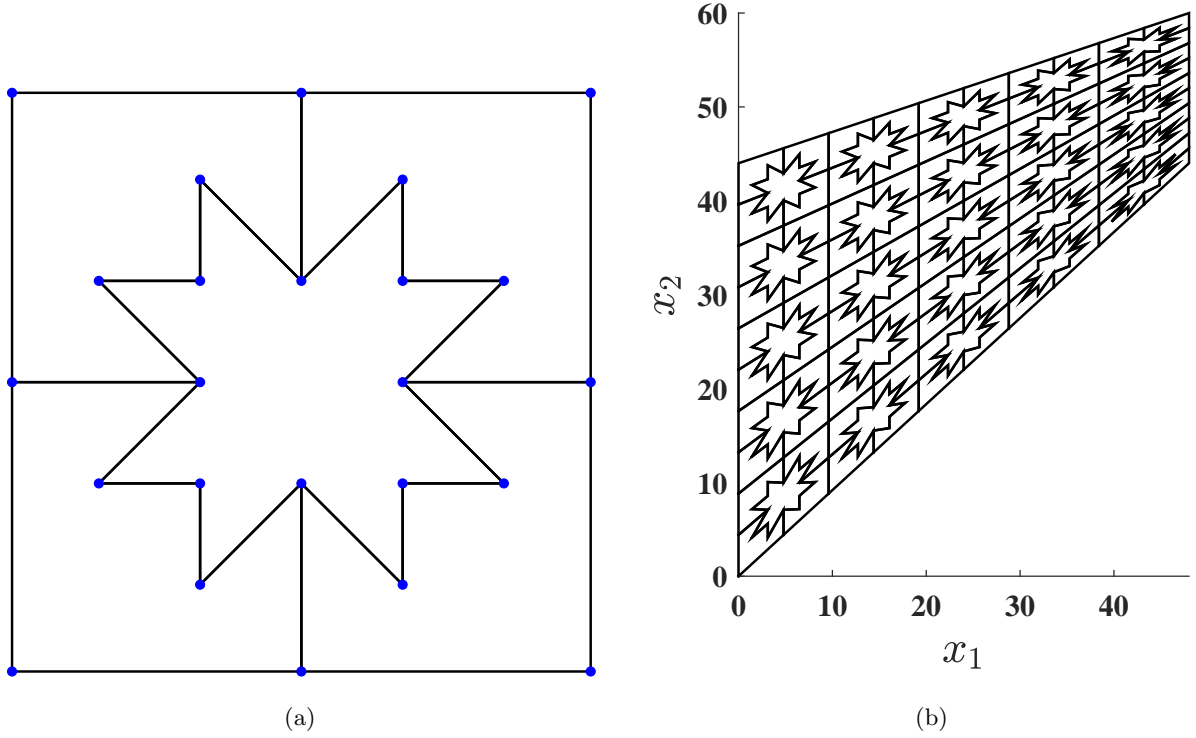


Fig. 10: Cook's membrane problem. (a) Master multielement. The center polygon defines an eight-point star known as 'Guñelve'; (b) a sample 'Guñelve' mesh.

The exact solution is given by [59]

$$\mathbf{u} = \begin{bmatrix} \frac{T}{4G} \left( \frac{\kappa+1}{2} r \cos \theta + \frac{r_0^2}{r} \left( (\kappa+1) \cos \theta + \cos 3\theta \right) - \frac{r_0^4}{r^3} \cos 3\theta \right) \\ \frac{T}{4G} \left( \frac{\kappa-3}{2} r \sin \theta + \frac{r_0^2}{r} \left( (\kappa-1) \sin \theta + \sin 3\theta \right) - \frac{r_0^4}{r^3} \sin 3\theta \right) \end{bmatrix},$$

where  $G = E_Y / (2(1 + \nu))$  and  $\kappa = (3 - \nu) / (1 + \nu)$ . The exact stress field is

$$\begin{bmatrix} \sigma_{11} \\ \sigma_{22} \\ \sigma_{12} \end{bmatrix} = \begin{bmatrix} T \left( 1 - \frac{r_0^2}{r^2} \left( \frac{3}{2} \cos 2\theta + \cos 4\theta \right) + \frac{3r_0^4}{2r^4} \cos 4\theta \right) \\ -T \left( \frac{r_0^2}{r^2} \left( \frac{1}{2} \cos 2\theta - \cos 4\theta \right) + \frac{3r_0^4}{2r^4} \cos 4\theta \right) \\ -T \left( \frac{r_0^2}{r^2} \left( \frac{1}{2} \sin 2\theta + \sin 4\theta \right) - \frac{3r_0^4}{2r^4} \sin 4\theta \right) \end{bmatrix},$$

where  $r$  is the radial distance from the center ( $x_1 = 0, x_2 = 0$ ) to a point  $(x_1, x_2)$  in the domain of analysis. In the computations, the following data are used:  $T = 100$ ,  $r_0 = 1$  and  $a = 5$ .

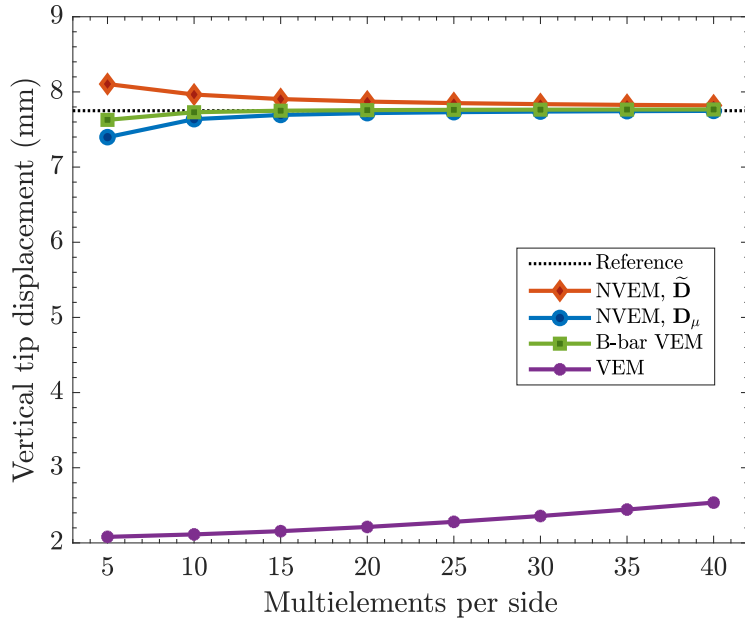


Fig. 11: Convergence of the vertical displacement at the tip of the Cook's membrane (point A) upon mesh refinement for the VEM, B-bar VEM and NVEM.

The Dirichlet boundary conditions on the domain of analysis (Fig. 15(b)) are imposed as follows:  $u_{1D} = 0$  on the left side and  $u_{2D} = 0$  on the bottom side. The Neumann boundary conditions are prescribed using the exact stresses, as follows:  $\mathbf{t}_N = [t_{1N} \ t_{2N}]^T = [\sigma_{12} \ \sigma_{22}]^T$  on the top side and  $\mathbf{t}_N = [t_{1N} \ t_{2N}]^T = [\sigma_{11} \ \sigma_{12}]^T$  on the right side.

In this example, regular, distorted and random meshes are used. For each of them, Fig. 16 shows a sample mesh. The random meshes are built using Polylla, a polygonal mesh generator [60]. Polylla generates meshes from any input triangulation (in this case, a Delaunay triangulation) using the longest-edge propagation path [61] and terminal-edge region concepts.

#### 6.4.1. Compressible elasticity

In terms of accuracy and convergence upon mesh refinement, Fig. 17 reveals that for the compressible case on regular meshes all the methods are accurate and converge optimally in the  $L^2$  norm and  $H^1$  seminorm of the displacement error, and the  $L^2$  norm of the pressure error (rates of 2, 1 and 1, respectively). In the  $L^2$  norm of the displacement error, the VEM and the B-bar VEM are more accurate than the NVEM. In the  $H^1$  seminorm of the displacement error and the

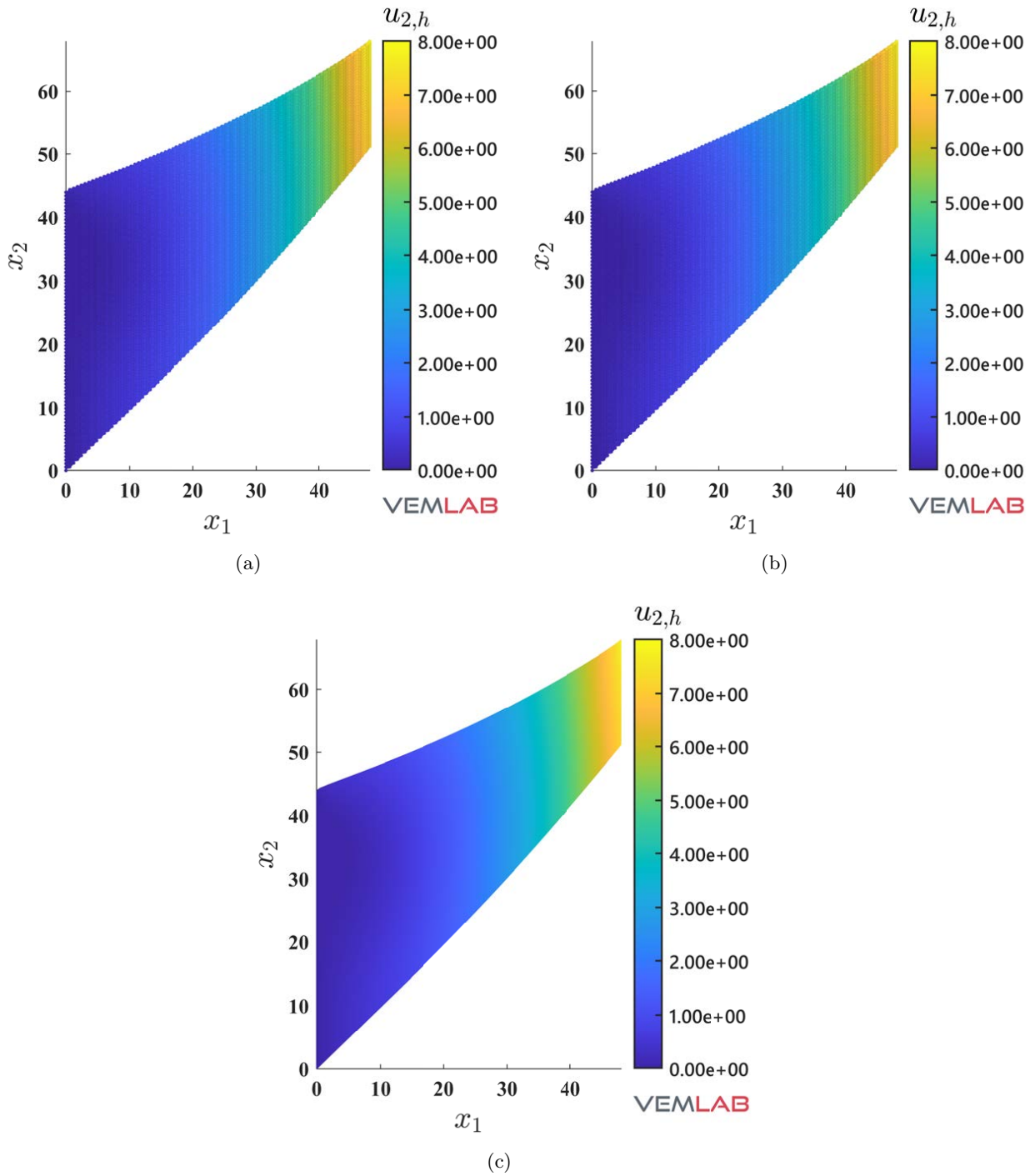


Fig. 12: Cook's membrane problem. Plots of the vertical displacement field solution ( $u_{2,h}$ ) for the (a) NVEM ( $\tilde{\mathbf{D}}$  stabilization), (b) NVEM ( $\mathbf{D}_\mu$  stabilization) and (c) B-bar VEM approaches. Plots are deformed according to  $u_{2,h}$ .

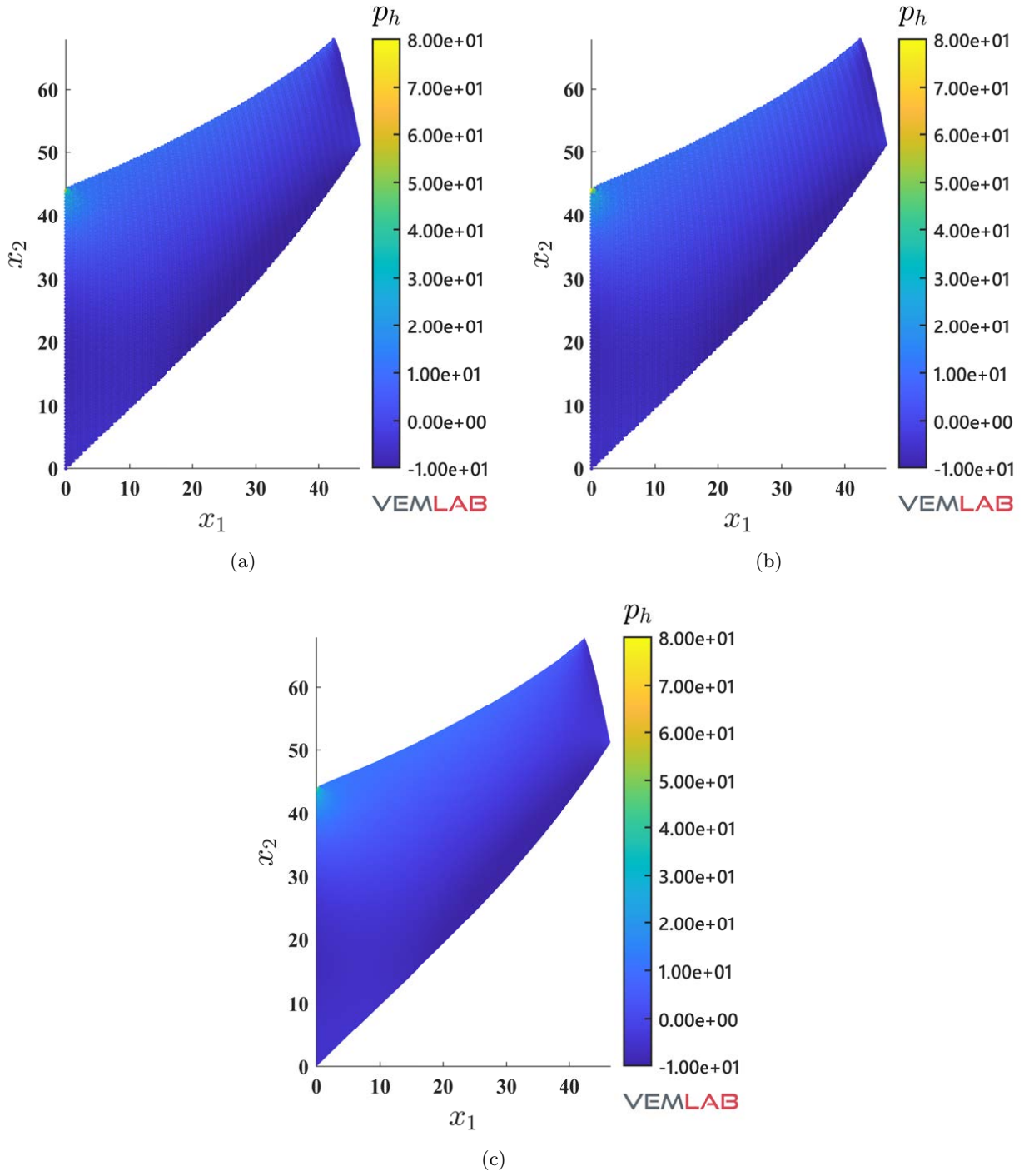


Fig. 13: Cook's membrane problem. Plots of the pressure field solution ( $p_h$ ) for the (a) NVEM ( $\tilde{\mathbf{D}}$  stabilization), (b) NVEM ( $\mathbf{D}_\mu$  stabilization) and (c) B-bar VEM approaches. Plots are deformed according to  $\|\mathbf{u}_h\|$ .

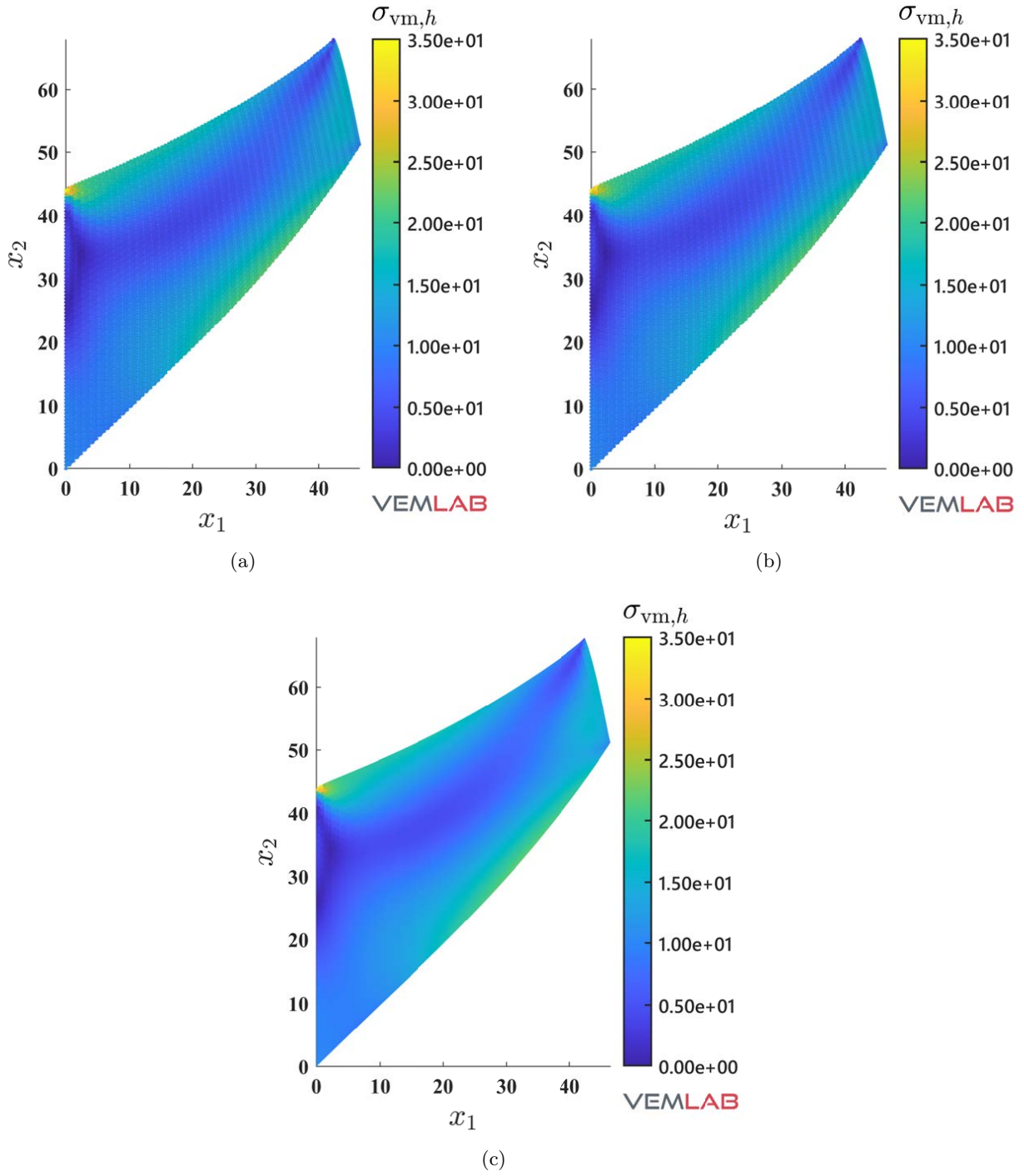


Fig. 14: Cook's membrane problem. Plots of the von Mises stress field solution ( $\sigma_{vm,h}$ ) for the (a) NVEM ( $\tilde{\mathbf{D}}$  stabilization), (b) NVEM ( $\mathbf{D}_\mu$  stabilization) and (c) B-bar VEM approaches. Plots are deformed according to  $\|\mathbf{u}_h\|$ .

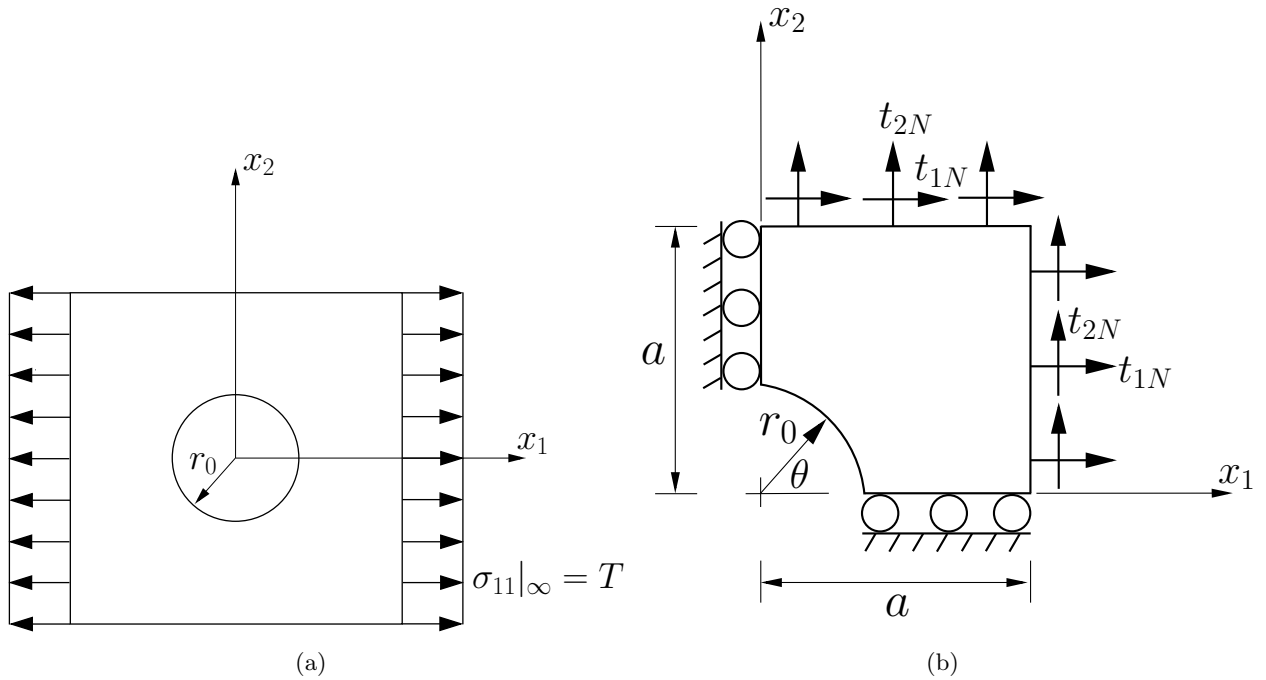


Fig. 15: Geometry and boundary conditions for the infinite plate with a circular hole. (a) Infinite domain and (b) a quarter of the domain.

$L^2$  norm of the pressure error, the VEM, the B-bar VEM and the NVEM with  $\tilde{\mathbf{D}}$  stabilization behave similar, while the NVEM with  $\mathbf{D}_\mu$  stabilization delivers the most accurate solution.

#### 6.4.2. Nearly incompressible elasticity

For the nearly incompressible case, regular, distorted and random meshes are considered. On regular and distorted meshes, the B-bar VEM and the NVEM are accurate and optimally convergent in the three norms (see Figs. 18 and 19), whereas, as expected, the VEM is severely inaccurate due to volumetric locking. In comparison with the B-bar VEM, Figs. 18 and 19 show that the NVEM is slightly more accurate in the  $H^1$  seminorm of the displacement error and the  $L^2$  norm of the pressure error, whereas less accurate in the  $L^2$  norm of the displacement error. We also observe that between the two stabilized NVEM, the NVEM with  $\mathbf{D}_\mu$  stabilization is slightly more accurate.

On random meshes, the B-bar VEM and the NVEM are accurate and optimally convergent in the three norms (Fig. 20), whereas the VEM is severely inaccurate due to volumetric locking.



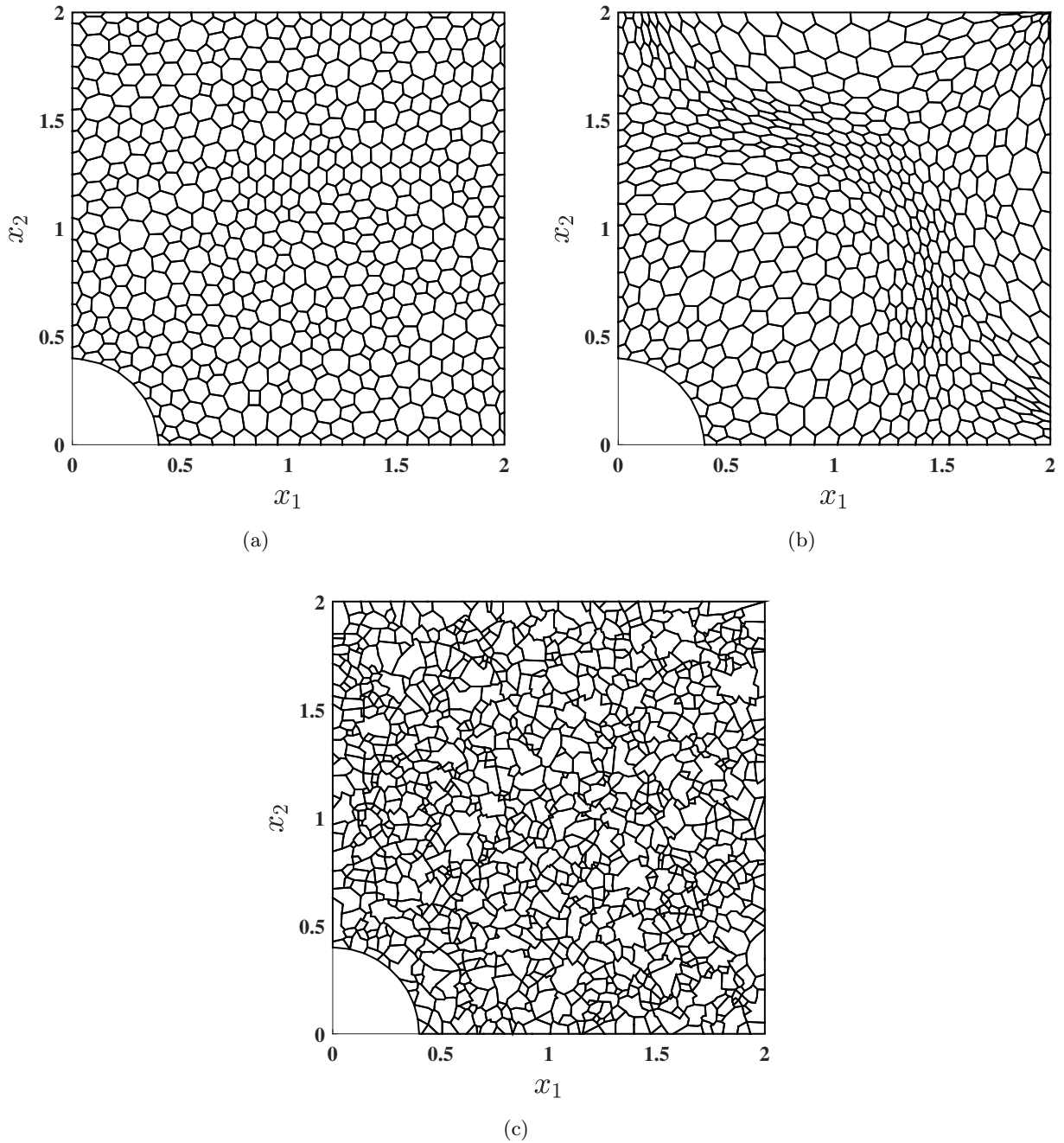


Fig. 16: Sample meshes for a quarter of the infinite plate with a circular hole. (a) Regular, (b) distorted and (c) random meshes.

Fig. 20(a) reveals that in the  $L^2$  norm of the displacement error the NVEM with  $\tilde{\mathbf{D}}$  stabilization is less accurate than the B-bar VEM, whereas slightly more accurate when  $\mathbf{D}_\mu$  stabilization is used. Regarding the  $H^1$  seminorm of the displacement error, Fig. 20(b) shows that the B-bar VEM and

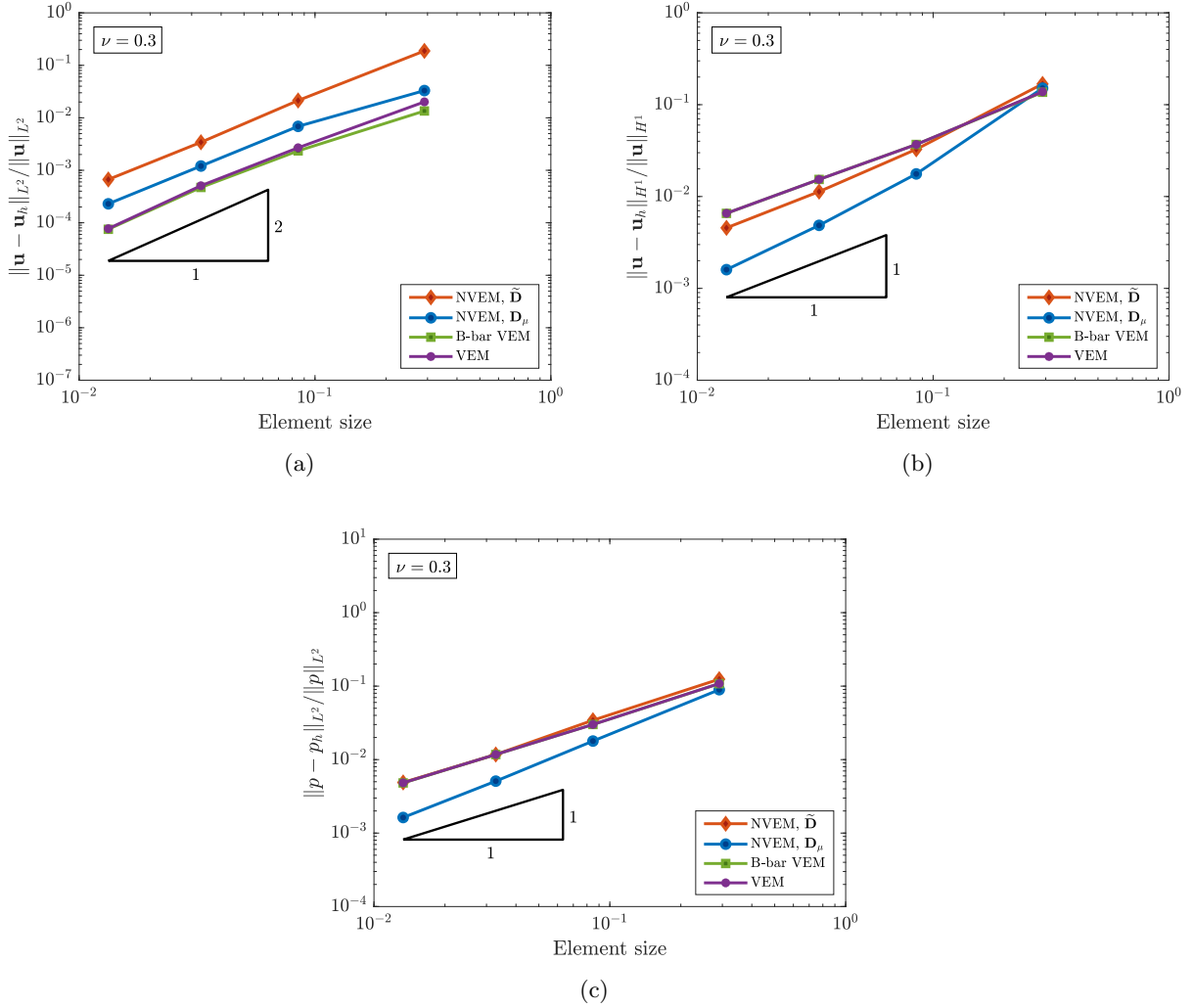


Fig. 17: Infinite plate with a circular hole problem on regular meshes. Material parameters  $E_Y = 10^3$  and  $\nu = 0.3$  for plane stress condition. Convergence rates in the (a)  $L^2$  norm of the displacement error, (b)  $H^1$  seminorm of the displacement error and (c)  $L^2$  norm of the pressure error for the VEM, B-bar VEM and NVEM.

the NVEM with  $\tilde{\mathbf{D}}$  stabilization behave similar, while the NVEM with  $\mathbf{D}_\mu$  stabilization is the most accurate. With respect to the  $L^2$  norm of the pressure error, the B-bar VEM is slightly more accurate than the NVEM approach (Fig. 20(c)).

Finally, plots of the displacement, pressure and von Mises stress fields are presented in Figs. 21, 22 and 23, respectively. Scatter plots are used for the NVEM as in this approach the field variables are known at the nodes. A very good agreement between the NVEM and the B-bar VEM solutions is found in these plots.

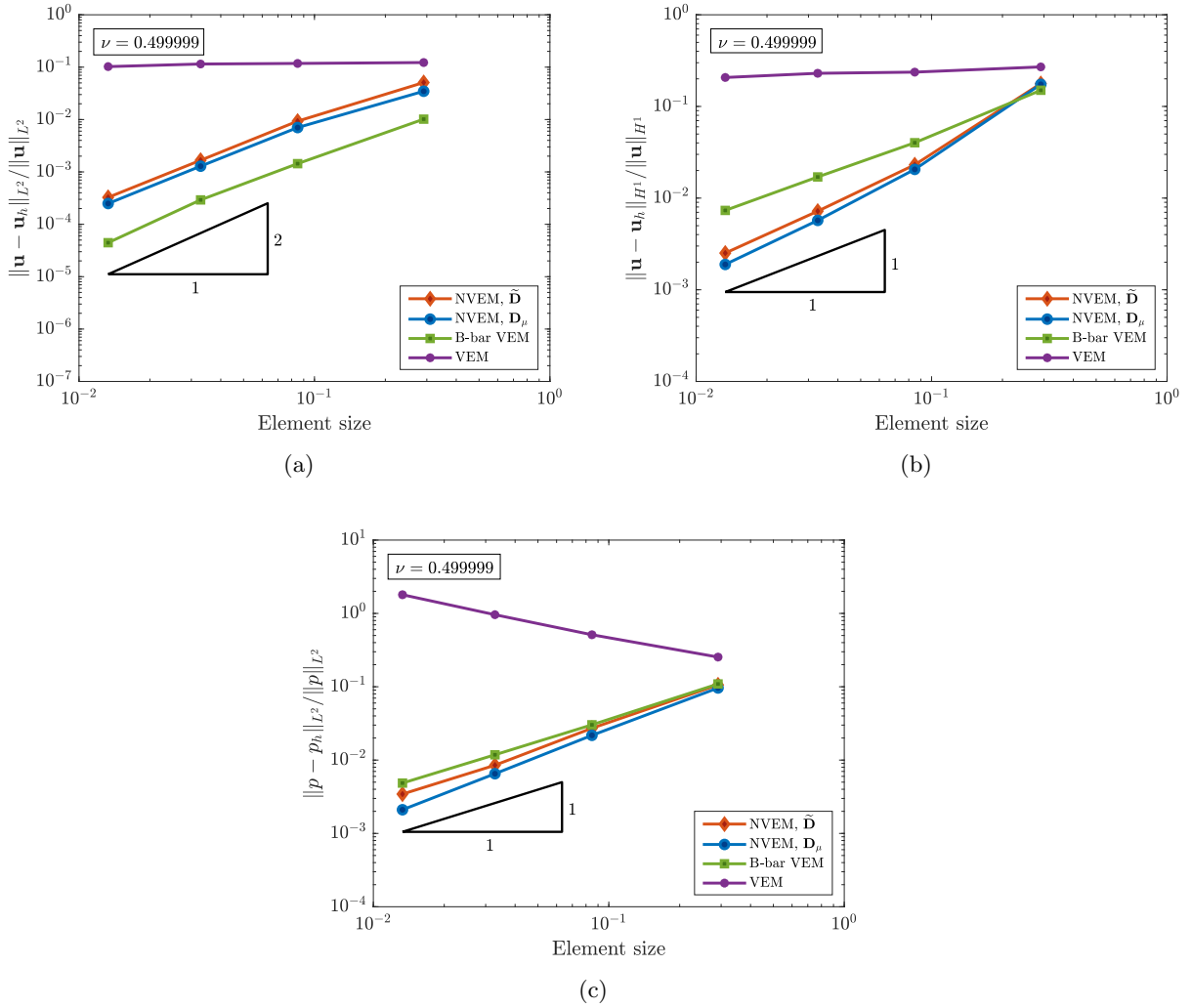


Fig. 18: Infinite plate with a circular hole problem (regular meshes). Material parameters  $E_Y = 10^3$  and  $\nu = 0.499999$  for plane strain condition. Convergence rates in the (a)  $L^2$  norm of the displacement error, (b)  $H^1$  seminorm of the displacement error and (c)  $L^2$  norm of the pressure error for the VEM, B-bar VEM and NVEM.

## 7. Concluding remarks

In this paper, we proposed a combined nodal integration and virtual element method, wherein the strain is averaged at the nodes from the strain of surrounding virtual elements. For the strain averaging procedure, a nodal averaging operator was constructed using a generalization to virtual elements of the node-based uniform strain approach for finite elements [30]. This gave rise to new virtual elements, which are termed node-based uniform strain virtual elements (NVEM). In line with nodal integration techniques, two stabilizations were proposed for the NVEM using modified

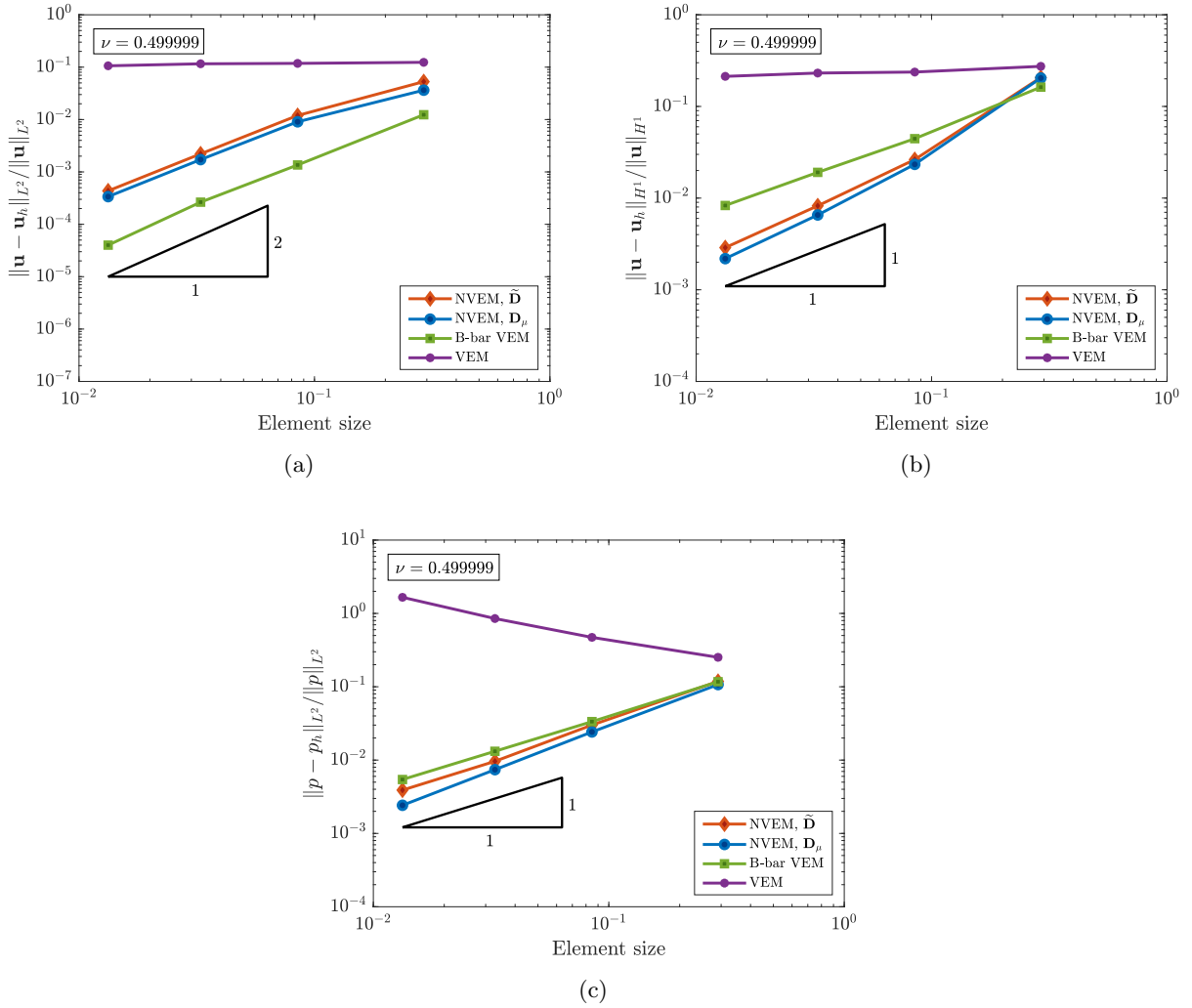


Fig. 19: Infinite plate with a circular hole problem (distorted meshes). Material parameters  $E_Y = 10^3$  and  $\nu = 0.499999$  for plane strain condition. Convergence rates in the (a)  $L^2$  norm of the displacement error, (b)  $H^1$  seminorm of the displacement error and (c)  $L^2$  norm of the pressure error for the VEM, B-bar VEM and NVEM.

constitutive matrices. The main distinction between the NVEM and existing VEM approaches for compressible and nearly incompressible elasticity, such as the B-Bar VEM [2], is that the stresses and strains in the NVEM are nodal variables just like displacements, whereas in the existing methods the stresses and strains are element variables.

Several examples in compressible and nearly incompressible elasticity were conducted using regular, distorted and random discretizations in two dimensions. The NVEM showed accurate, convergent and stable solutions in the  $L^2$  norm and  $H^1$  seminorm of the displacement error in all the

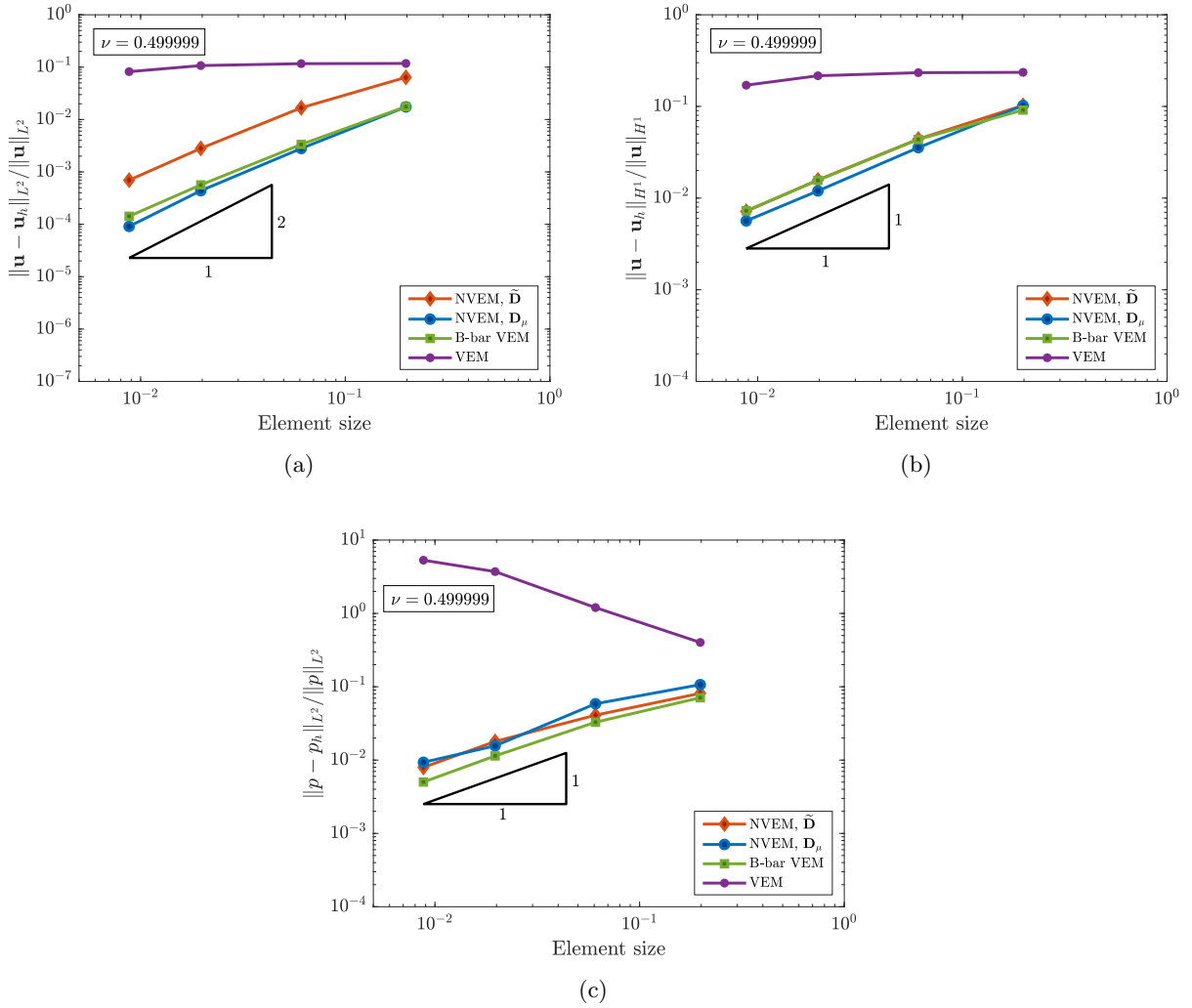


Fig. 20: Infinite plate with a circular hole problem (random meshes). Material parameters  $E_Y = 10^3$  and  $\nu = 0.499999$  for plane strain condition. Convergence rates in the (a)  $L^2$  norm of the displacement error, (b)  $H^1$  seminorm of the displacement error and (c)  $L^2$  norm of the pressure error for the VEM, B-bar VEM and NVEM.

numerical tests. Even though the NVEM and the B-Bar VEM behave similar in terms of accuracy and convergence, we remark that all the field variables in the NVEM are related to the nodes, which would obviously ease the tracking of the state and history-dependent variables in the nonlinear regime. Also, the nodal character of these variables can be exploited in extreme deformations settings, where, if remeshing is needed, a remeshing strategy using the current set of nodes would eliminate the necessity of remapping of the state and history-dependent variables between the old and new meshes. The aforementioned features provide room for further development of the

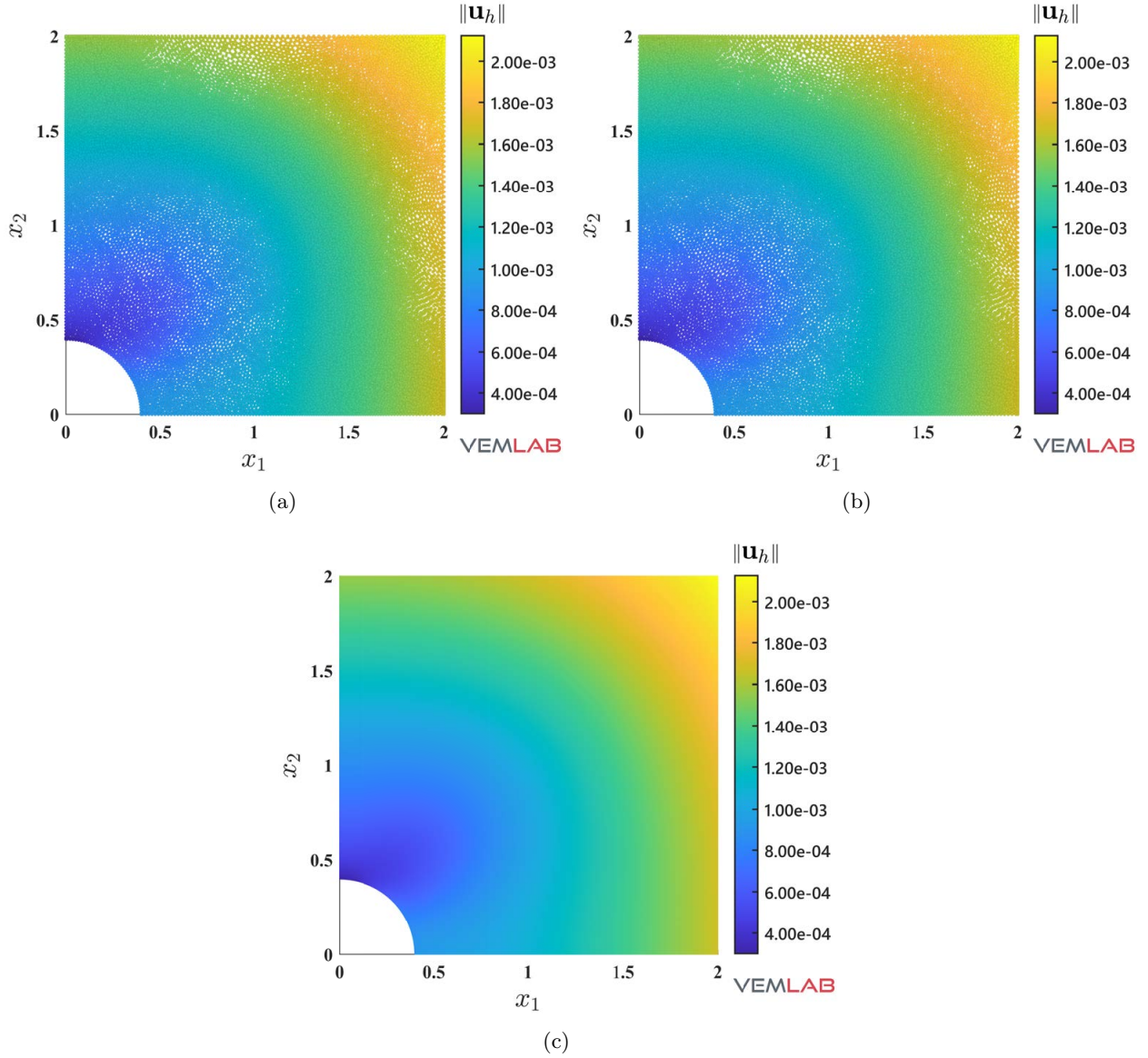


Fig. 21: Infinite plate with a circular hole problem. Material parameters  $E_Y = 10^3$  and  $\nu = 0.499999$  for plane strain condition. Plots of the norm of the displacement field solution ( $\|\mathbf{u}_h\|$ ) for the (a) NVEM ( $\tilde{\mathbf{D}}$  stabilization), (b) NVEM ( $\mathbf{D}_\mu$  stabilization) and (c) B-bar VEM approaches.

NVEM. In a short term view, our current work on the NVEM is focused on its extension to materially-nonlinear-only formulation. In the medium term, we plan to develop its extension to finite deformations.

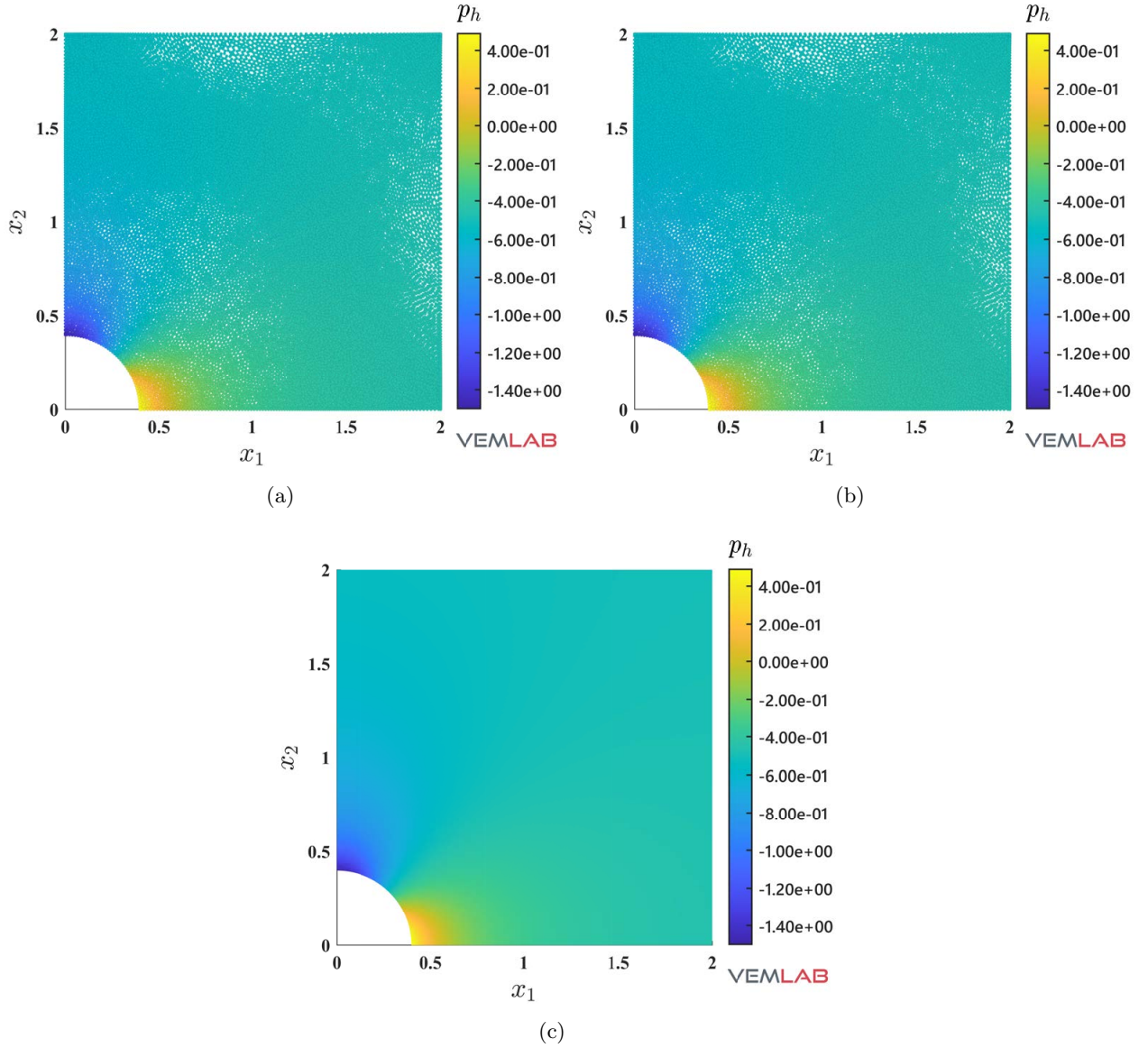


Fig. 22: Infinite plate with a circular hole problem. Material parameters  $E_Y = 10^3$  and  $\nu = 0.499999$  for plane strain condition. Plots of the pressure field solution ( $p_h$ ) for the (a) NVEM ( $\tilde{\mathbf{D}}$  stabilization), (b) NVEM ( $\mathbf{D}_\mu$  stabilization) and (c) B-bar VEM approaches.

## Acknowledgements

This work was performed under the auspices of the Chilean National Fund for Scientific and Technological Development (FONDECYT) through grants ANID FONDECYT No. 1221325 (A.O-B and R.S-V) and ANID FONDECYT No. 1211484 (N.H-K). S.S-F gratefully acknowledges the research support of the Chilean National Agency of Research and Development (ANID) through



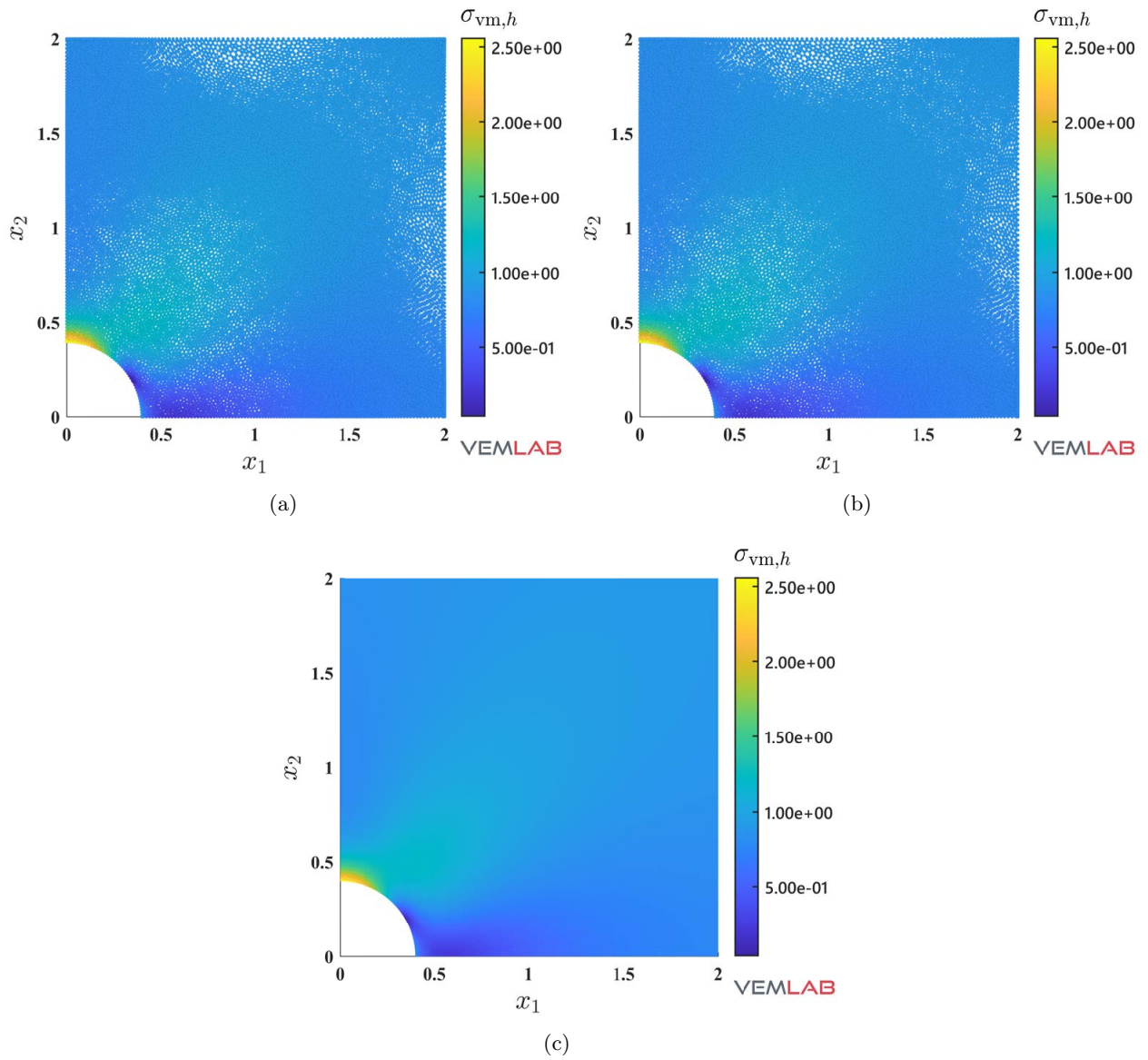


Fig. 23: Infinite plate with a circular hole problem. Material parameters  $E_Y = 10^3$  and  $\nu = 0.499999$  for plane strain condition. Plots of the von Mises stress field solution ( $\sigma_{vm,h}$ ) for the (a) NVEM ( $\tilde{\mathbf{D}}$  stabilization), (b) NVEM ( $\mathbf{D}_\mu$  stabilization) and (c) B-bar VEM approaches.

grant ANID doctoral scholarship No. 21202379.



## Appendix A. List of main symbols

$\mathbf{b}$	body force vector
$\widehat{\mathbf{b}}$	element average of the body force vector
$\widehat{\mathbf{b}}_I$	nodal average of $\widehat{\mathbf{b}}$
$\mathbf{D}$	constitutive matrix for the linear elastic material
$\widetilde{\mathbf{D}}$	modified constitutive matrix for the linear elastic material
$\mathbf{D}_\mu$	modified constitutive matrix for the linear elastic material
$E$	element or domain of the element
$e$	edge of an element
$ E $	area of the element
$ e $	length of an element edge
$E_Y$	Young's modulus of the linear elastic material
$\mathbf{f}_E^b$	VEM element force vector associated with $\mathbf{b}$
$\mathbf{f}_I^b$	NVEM nodal force vector associated with $\mathbf{b}$
$\mathbf{f}_e^t$	VEM element force vector associated with $\mathbf{t}_N$
$\mathbf{f}_I^t$	NVEM nodal force vector associated with $\mathbf{t}_N$
$I$	a node of the mesh
$ I $	representative area of node $I$
$\mathbf{K}_E$	VEM element stiffness matrix
$\mathbf{K}_I$	NVEM nodal stiffness matrix
$\mathbf{K}_E^c$	consistency part of the VEM element stiffness matrix
$\mathbf{K}_I^c$	consistency part of the NVEM nodal stiffness matrix
$\mathbf{K}_E^s$	stability part of the VEM element stiffness matrix
$\mathbf{K}_I^s$	stability part of the NVEM nodal stiffness matrix
$\mathbf{n}$	unit outward normal to the element boundary
$\mathbf{n}_a$	unit outward normal to the $a$ -th edge of the element
$\mathbf{n}_\Gamma$	unit outward normal to the domain boundary
$N_E^V$	number of edges/nodes of an element

$N_e^V$	number of nodes of an element edge
$\mathbf{t}_N$	Neumann boundary condition
$\widehat{\mathbf{t}}_N$	edge average of the Neumann boundary condition
$\widehat{\mathbf{t}}_{N,I}$	nodal average of $\widehat{\mathbf{t}}_N$
$\mathbf{u}$	displacement vector
$\mathbf{u}_D$	Dirichlet boundary condition
$\mathbf{u}_h$	discrete trial displacement vector
$\mathbf{u}_a$	nodal displacement vector
$\bar{\mathbf{u}}$	mean of the values that $\mathbf{u}$ takes over the vertices of an element
$\mathbf{v}$	virtual displacement vector
$\mathbf{v}_h$	discrete test displacement vector
$\mathbf{x}$	position vector
$\mathbf{x}_a$	nodal coordinates
$\bar{\mathbf{x}}$	mean of the values that $\mathbf{x}$ takes over the vertices of an element
$\boldsymbol{\varepsilon}$	small strain tensor
$\widehat{\boldsymbol{\varepsilon}}$	element average of the small strain tensor
$\boldsymbol{\varepsilon}_I$	nodal strain tensor
$\partial E$	boundary of the element
$\Gamma$	boundary of the body
$\Gamma_D$	Dirichlet boundary
$\Gamma_N$	Neumann boundary
$\lambda$	Lamé's first parameter
$\mu$	Lamé's second parameter (shear modulus of the linear elastic material)
$\nu$	Poisson's ratio of the linear elastic material
$\Omega$	domain of the body
$\boldsymbol{\omega}$	small rotation tensor
$\widehat{\boldsymbol{\omega}}$	element average of the small rotation tensor
$\boldsymbol{\sigma}$	Cauchy stress tensor

## References

- [1] K. Park, H. Chi, G. H. Paulino, Numerical recipes for elastodynamic virtual element methods with explicit time integration, *International Journal for Numerical Methods in Engineering* 121 (1) (2020) 1–31.
- [2] K. Park, H. Chi, G. H. Paulino, B-bar virtual element method for nearly incompressible and compressible materials, *Meccanica* 56 (6) (2021) 1423–1439.
- [3] E. Artioli, S. de Miranda, C. Lovadina, L. Patruno, A stress/displacement virtual element method for plane elasticity problems, *Computer Methods in Applied Mechanics and Engineering* 325 (2017) 155–174.
- [4] A. D’Altri, S. de Miranda, L. Patruno, E. Sacco, An enhanced vem formulation for plane elasticity, *Computer Methods in Applied Mechanics and Engineering* 376 (2021) 113663.
- [5] F. Dassi, C. Lovadina, M. Visinoni, Hybridization of the virtual element method for linear elasticity problems, *Mathematical Models and Methods in Applied Sciences* 31 (14) (2021) 2979–3008.
- [6] D. Y. Kwak, H. Park, Lowest-order virtual element methods for linear elasticity problems, *Computer Methods in Applied Mechanics and Engineering* 390 (2022) 114448.
- [7] B. Zhang, J. Zhao, Y. Yang, S. Chen, The nonconforming virtual element method for elasticity problems, *Journal of Computational Physics* 378 (2019) 394–410.
- [8] Y. Yu, A lowest-order locking-free nonconforming virtual element method based on the reduced integration technique for linear elasticity problems (2021). [doi:10.48550/ARXIV.2112.13378](https://doi.org/10.48550/ARXIV.2112.13378).
- [9] X. Tang, Z. Liu, B. Zhang, M. Feng, A low-order locking-free virtual element for linear elasticity problems, *Computers & Mathematics with Applications* 80 (5) (2020) 1260–1274.
- [10] S. Beissel, T. Belytschko, Nodal integration of the element-free Galerkin method, *Computer Methods in Applied Mechanics and Engineering* 139 (1) (1996) 49–74.
- [11] M. A. Puso, J.-S. Chen, E. Zywicz, W. Elmer, Meshfree and finite element nodal integration methods, *International Journal for Numerical Methods in Engineering* 74 (3) (2008) 416–446.
- [12] T. Belytschko, S. Xiao, Stability analysis of particle methods with corrected derivatives, *Computers & Mathematics with Applications* 43 (3–5) (2002) 329–350.
- [13] T. P. Fries, T. Belytschko, Convergence and stabilization of stress-point integration in mesh-free and particle methods, *International Journal for Numerical Methods in Engineering* 74 (7) (2008) 1067–1087.
- [14] T. Belytschko, Y. Guo, W. K. Liu, S. P. Xiao, A unified stability analysis of meshless particle methods, *International Journal for Numerical Methods in Engineering* 48 (9) (2000) 1359–1400.
- [15] M. Hillman, J.-S. Chen, An accelerated, convergent, and stable nodal integration in Galerkin meshfree methods for linear and nonlinear mechanics, *International Journal for Numerical Methods in Engineering* 107 (7) (2016) 603–630.
- [16] J.-S. Chen, M. Hillman, M. Rüter, An arbitrary order variationally consistent integration for Galerkin meshfree methods, *International Journal for Numerical Methods in Engineering* 95 (5) (2013) 387–418.

- [17] M. A. Puso, J. Solberg, A stabilized nodally integrated tetrahedral, *International Journal for Numerical Methods in Engineering* 67 (6) (2006) 841–867.
- [18] J.-S. Chen, C. T. Wu, S. Yoon, Y. You, A stabilized conforming nodal integration for Galerkin mesh-free methods, *International Journal for Numerical Methods in Engineering* 50 (2) (2001) 435–466.
- [19] J.-S. Chen, S. Yoon, C. T. Wu, Non-linear version of stabilized conforming nodal integration for Galerkin mesh-free methods, *International Journal for Numerical Methods in Engineering* 53 (12) (2002) 2587–2615.
- [20] W. Elmer, J. S. Chen, M. Puso, E. Taciroglu, A stable, meshfree, nodal integration method for nearly incompressible solids, *Finite Elements in Analysis and Design* 51 (2012) 81–85.
- [21] R. Silva-Valenzuela, A. Ortiz-Bernardin, N. Sukumar, E. Artioli, N. Hitschfeld-Kahler, A nodal integration scheme for meshfree galerkin methods using the virtual element decomposition, *International Journal for Numerical Methods in Engineering* 121 (10) (2020) 2174–2205.
- [22] Q. Duan, B. Wang, X. Gao, X. Li, Quadratically consistent nodal integration for second order meshfree Galerkin methods, *Computational Mechanics* 54 (2) (2014) 353–368.
- [23] P. Lancaster, K. Salkauskas, Surfaces generated by moving least squares methods, *Mathematics of Computations* 37 (1981) 141–158.
- [24] T. Belytschko, Y. Y. Lu, L. Gu, Element-free Galerkin methods, *International Journal for Numerical Methods in Engineering* 37 (2) (1994) 229–256.
- [25] W. K. Liu, S. Jun, Y. F. Zhang, Reproducing kernel particle methods, *International Journal for Numerical Methods in Engineering* 20 (8–9) (1995) 1081–1106.
- [26] N. Sukumar, Construction of polygonal interpolants: a maximum entropy approach, *International Journal for Numerical Methods in Engineering* 61 (12) (2004) 2159–2181.
- [27] N. Sukumar, R. W. Wright, Overview and construction of meshfree basis functions: from moving least squares to entropy approximants, *International Journal for Numerical Methods in Engineering* 70 (2) (2007) 181–205.
- [28] M. Arroyo, M. Ortiz, Local maximum-entropy approximation schemes: a seamless bridge between finite elements and meshfree methods, *International Journal for Numerical Methods in Engineering* 65 (13) (2006) 2167–2202.
- [29] J. Bonet, A. J. Burton, A simple average nodal pressure tetrahedral element for incompressible and nearly incompressible dynamic explicit applications, *Communications in Numerical Methods in Engineering* 14 (5) (1998) 437–449.
- [30] C. R. Dohrmann, M. W. Heinstein, J. Jung, S. W. Key, W. R. Witkowski, Node-based uniform strain elements for three-node triangular and four-node tetrahedral meshes, *International Journal for Numerical Methods in Engineering* 47 (9) (2000) 1549–1568.
- [31] J. Bonet, H. Marriott, O. Hassan, An averaged nodal deformation gradient linear tetrahedral element for large strain explicit dynamic applications, *Communications in Numerical Methods in Engineering* 17 (8) (2001) 551–561.
- [32] P. Krysl, B. Zhu, Locking-free continuum displacement finite elements with nodal integration, *International*

- Journal for Numerical Methods in Engineering 76 (7) (2008) 1020–1043.
- [33] G. Castellazzi, P. Krysl, Displacement-based finite elements with nodal integration for reissner–mindlin plates, *International Journal for Numerical Methods in Engineering* 80 (2) (2009) 135–162.
- [34] P. Krysl, H. Kagey, Reformulation of nodally integrated continuum elements to attain insensitivity to distortion, *International Journal for Numerical Methods in Engineering* 90 (7) (2012) 805–818.
- [35] G. Castellazzi, P. Krysl, Patch-averaged assumed strain finite elements for stress analysis, *International Journal for Numerical Methods in Engineering* 90 (13) (2012) 1618–1635.
- [36] M. Broccardo, M. Micheloni, P. Krysl, Assumed-deformation gradient finite elements with nodal integration for nearly incompressible large deformation analysis, *International Journal for Numerical Methods in Engineering* 78 (9) (2009) 1113–1134.
- [37] G. Castellazzi, P. Krysl, I. Bartoli, A displacement-based finite element formulation for the analysis of laminated composite plates, *Composite Structures* 95 (2013) 518–527.
- [38] E. Artioli, G. Castellazzi, P. Krysl, Assumed strain nodally integrated hexahedral finite element formulation for elastoplastic applications, *International Journal for Numerical Methods in Engineering* 99 (11) (2014) 844–866.
- [39] A. Franci, M. Cremonesi, U. Perego, E. O. nate, A lagrangian nodal integration method for free-surface fluid flows, *Computer Methods in Applied Mechanics and Engineering* 361 (2020) 112816.
- [40] J. Meng, X. Zhang, S. Utili, E. O. nate, A nodal-integration based particle finite element method (N-PFEM) to model cliff recession, *Geomorphology* 381 (2021) 107666.
- [41] S. Berrone, A. Borio, F. Marcon, Comparison of standard and stabilization free virtual elements on anisotropic elliptic problems, *Applied Mathematics Letters* 129 (2022) 107971.
- [42] A. Chen, N. Sukumar, Stabilization-free virtual element method for plane elasticity (2022). [doi:10.48550/ARXIV.2202.10037](https://doi.org/10.48550/ARXIV.2202.10037).
- [43] A. Ortiz-Bernardin, C. Alvarez, N. Hitschfeld-Kahler, A. Russo, R. Silva-Valenzuela, E. Olate-Sanzana, Veamy: an extensible object-oriented C++ library for the virtual element method, *Numerical Algorithms* 82 (4) (2019) 1189–1220.
- [44] E. Artioli, L. Beirão da Veiga, C. Lovadina, E. Sacco, Arbitrary order 2D virtual elements for polygonal meshes: part I, elastic problem, *Computational Mechanics* 60 (3) (2017) 355–377.
- [45] E. Artioli, L. Beirão da Veiga, C. Lovadina, E. Sacco, Arbitrary order 2D virtual elements for polygonal meshes: part II, inelastic problem, *Computational Mechanics* 60 (4) (2017) 643–657.
- [46] P. Wriggers, B. D. Reddy, W. Rust, B. Hudobivnik, Efficient virtual element formulations for compressible and incompressible finite deformations, *Computational Mechanics* 60 (2) (2017) 253–268.
- [47] L. Beirão da Veiga, F. Dassi, A. Russo, High-order virtual element method on polyhedral meshes, *Computers & Mathematics with Applications* 74 (5) (2017) 1110–1122.
- [48] L. Beirão da Veiga, F. Brezzi, F. Dassi, L. D. Marini, A. Russo, Serendipity virtual elements for general elliptic equations in three dimensions, *Chinese Annals of Mathematics, Series B* 39 (2018) 315–334.

- [49] K. Park, H. Chi, G. H. Paulino, On nonconvex meshes for elastodynamics using virtual element methods with explicit time integration, *Computer Methods in Applied Mechanics and Engineering* 356 (2019) 669–684.
- [50] H. Chi, L. B. da Veiga, G. Paulino, Some basic formulations of the virtual element method (VEM) for finite deformations, *Computer Methods in Applied Mechanics and Engineering* 318 (2017) 148–192.
- [51] A. L. Gain, G. H. Paulino, Bridging art and engineering using escher-based virtual elements, *Structural and Multidisciplinary Optimization* 51 (2015) 867–883.
- [52] L. Beirão da Veiga, F. Brezzi, A. Cangiani, G. Manzini, L. D. Marini, A. Russo, Basic principles of virtual element methods, *Mathematical Models and Methods in Applied Sciences* 23 (1) (2013) 199–214.
- [53] A. L. Gain, C. Talischi, G. H. Paulino, On the virtual element method for three-dimensional linear elasticity problems on arbitrary polyhedral meshes, *Computer Methods in Applied Mechanics and Engineering* 282 (2014) 132–160.
- [54] A. Ortiz-Bernardin, A. Russo, N. Sukumar, Consistent and stable meshfree Galerkin methods using the virtual element decomposition, *International Journal for Numerical Methods in Engineering* 112 (7) (2017) 655–684.
- [55] L. Beirão da Veiga, F. Brezzi, L. D. Marini, Virtual elements for linear elasticity problems, *SIAM Journal on Numerical Analysis* 51 (2) (2013) 794–812.
- [56] F. M. Andrade Pires, E. A. de Souza Neto, J. L. de la Cuesta Padilla, An assessment of the average nodal volume formulation for the analysis of nearly incompressible solids under finite strains, *Communications in Numerical Methods in Engineering* 20 (7) (2004) 569–583.
- [57] L. Mascotto, Ill-conditioning in the virtual element method: Stabilizations and bases, *Numerical Methods for Partial Differential Equations* 34 (4) (2018) 1258–1281.
- [58] H. C. Elman, D. J. Silvester, A. J. Wathen, *Finite Elements and Fast Iterative Solvers: with Applications in Incompressible Fluid Dynamics*, Oxford University Press, Inc, NY, 2006.
- [59] S. P. Timoshenko, J. N. Goodier, *Theory of Elasticity*, 3rd Edition, McGraw-Hill, NY, 1970.
- [60] S. Salinas, N. Hitschfeld-Kahler, A. Ortiz-Bernardin, H. Si, Polylla: Polygonal meshing algorithm based on terminal-edge regions, *Engineering with Computers* (2022). doi:10.1007/s00366-022-01643-4.
- [61] M.-C. Rivara, New longest-edge algorithms for the refinement and/or improvement of unstructured triangulations, *International Journal for Numerical Methods in Engineering* 40 (18) (1997) 3313–3324.